USING MINERAL EQUILIBRIA TO ESTIMATE H_2O ACTIVITIES IN PERIDOTITES FROM THE WESTERN GNEISS REGION OF NORWAY

A Thesis

by

PATRICIA KANG

Submitted to the Office of Graduate and Professional Studies of
Texas A&M University
in partial fulfillment of the requirements for the degree of

MASTER OF SCIENCE

Chair of Committee,	Will Lamb
Committee Members,	Andreas Kronenberg
	Julie Newman
	Debbie Thomas
Head of Department,	Rick Giardino

May 2015

Major Subject: Geology

ABSTRACT

The earth's mantle is an important reservoir of H_2O, and even a small amount of H_2O has a significant influence on the physical properties of mantle rocks. Estimating the amount of H_2O in rocks from the earth's mantle would, therefore, provide some insights into the physical properties of this volumetrically dominant portion of the earth. The goal of this study is to use mineral equilibria to determine the activities of H_2O (aH_2O) in samples derived from the mantle. Two different approaches are applied to estimate H_2O activities in orogenic mantle peridotites from the Western Gneiss Region of Norway. The first approach uses amphibole dehydration equilibrium as described by Lamb and Popp (2009). The second approach is to estimate the minimum value of aH_2O by characterizing fluid speciation in C-O-H system for a given value of oxygen fugacity (fO_2). Values of fO_2 were estimated from a fO_2-buffering reaction between olivine, orthopyroxene, and spinel (Wood, 1990). Our results show that the estimate of aH_2O obtained from the amphibole dehydration equilibrium is significantly lower than that estimated from the C-O-H calculation. This indicates that fluid pressure (P_{fluid}) is less than lithostatic pressure (P_{lith}) which, for metamorphic rocks, implies the absence of a free fluid phase.

Fluid absent condition could be generated by amphibole growth during exhumation. If small amounts of H_2O were added to these rocks, the formation of amphibole could yield low values of aH_2O by consuming all available H_2O. On the other hand, if H_2O infiltrated at P-T conditions outside of the stability field of amphibole, the

nominally anhydrous minerals (NAMs) might have served as a reservoir of H_2O. In this case, NAMs could supply the OH necessary for amphibole growth once retrograde P-T conditions were consistent with amphibole stability. Thus, amphibole growth may effectively dehydrate co-existing NAMs, and enhance the strength of rocks as long as the NAMs controlled the rheology of the rock.

ACKNOWLEDGEMENTS

I would like to thank my committee chair, Dr. Lamb, and my committee members, Dr. Kronenberg, Dr. Newman, and Dr. Thomas, for their guidance and support throughout the course of this research.

Thanks also go to my friends and colleagues and the department faculty for making my time at Texas A&M University a great experience.

Finally, thanks to my family for their encouragement and love.

TABLE OF CONTENTS

Page

LIST OF FIGURES

Page

LIST OF TABLES

Page

1. INTRODUCTION

H_2O has a significant influence on the physical properties of mantle rocks. For instance, H_2O enhances ionic diffusion rate, thereby reducing the effective viscosity of mantle minerals (Hirth and Kohlstedt, 1996; Mei and Kohlstedt, 2000a, 2000b; Karato and Jung, 2003). Given that modeling convection in the mantle requires constraints on viscosity (Solomatov, 1995; Moresi and Solomatov, 1998; Tackley, 1998), estimates of mantle H_2O content are required to model convection and determine the threshold amount of H_2O for the operation of plate tectonic style of convection (Moresi and Solomatov, 1998).

Seismic discontinuities, consistent with the mantle phase transformation boundaries, are affected by the presence of water (Wood, 1995). As an example, H_2O can shift the phase boundary of olivine and wadsleyite to lower pressure, and therefore do so for the 410km seismic discontinuity (Wood, 1995). Moreover, H_2O can account for the high conductivity anomalies in the upper mantle and the transition zone, since it can provide free protons as an additional conductive phase (Tarits et al., 2004; Koyama et al., 2006).

The H_2O content of various mantle rocks has been characterized based on the amount of H in nominally anhydrous minerals (NAMs), such as olivine, pyroxene, and garnet (e.g., Skogby et al., 1990; Peslier et al., 2002; Bell et al., 2003; Maldener et al., 2003). While this approach may provide insight into mantle H_2O contents, a potential confounding effect is the possible diffusive loss of hydrogen during the emplacement of

mantle rocks at the surface of the earth. This may be a problem for olivine contained in mantle xenoliths (e.g., Ingrin and Skogby, 2000; Demouchy and Mackwell, 2006) even though these rocks have undergone rapid uplift and cooling as compared orogenic peridotities. Diffusion rates of H_2O in pyroxenes are probably significantly less than those in olivine (Bai and Kohlstedt, 1992, 1993) and Warren and Hauri (2014) argue that pyroxenes from orogenic peridotites may retain their pre-emplacement H content while olivine from the same rocks may suffer significant H-loss.

H_2O buffering amphibole (pargasite) dehydration equilibrium have also been used to estimate the activity of H_2O (aH_2O) in the mantle. For example, Lamb and Popp (2009) estimated the activities of H_2O from amphibole dehydration equilibria, and they were in good agreement with those inferred from a combination of hydrogen fugacities and oxygen fugacities, obtained from oxy-amphibole equilibria (Popp et al., 2006) and the oxybarometer of Wood (1990), respectively (Lamb and Popp, 2009). These results indicate that values of aH_2O estimated from amphibole equilibria are not sensitive to partial H-loss from amphibole via diffusion (Lamb and Popp, 2009). Thus, this paper applied amphibole (pargasite) dehydration equilibrium to estimate values of aH_2O in orogenic mantle peridotites. This study also determined values of oxygen fugacity (fO_2) via the O_2-buffering equilibrium between olivine, orthopyroxene, and spinel (Wood, 1990). Values of fO_2 were used to constrain the activities of a variety of fluid species in the C-O-H system, including H_2O, CO_2, CH_4, H_2, and CO (Zhang and Duan, 2009; Lamb and Valley, 1984, 1985), and yielded insight into the possibility of mineral equilibration in the absence of lithostatically pressured fluid phase (Lamb and Valley, 1984, 1985).

2. GEOLOGICAL AND PETROLOGICAL BACKGROUND

The Western Gneiss Region (WGR) of Norway is part of the Norwegian Caledonides which covers an area of approximately $5 \times 10^4 km^2$ between Bergen and Trondheim (Fig. 1). The WGR lies within a tectonic window and is surrounded by thick piles of allochthonous tectonic nappes which migrated eastwards onto Baltica during the continental collision between Baltica and Laurentia (Roberts and Gee, 1985). The subduction of Baltica, which occurred during the Scandian orogeny, produced minerals which are stable under ultra-high pressure (UHP) metamorphic conditions (Smith, 1984; Van Roermund et al., 2002; Vrijmoed et al., 2006; Brueckner et al., 2002).

A number of orogenic garnet peridotites are exposed within the WGR (Carswell, 1986; Drury et al., 2001; Spengler et al., 2006; Van Roermund, 2009). The amphibole-bearing mineral assemblages investigated in this study likely formed during cooling and depressurization following the UHP event (see the following discussion). However, in rare cases, peridotites from this region contain mineral assemblages that date from Archean and Proterozoic. For example, certain garnet-bearing orogenic peridotites exposed on the Otrøy Island contain megacrystic olivine and orthopyroxene as well as supersilicic garnet with 20% of majoritic component (Spengler et al., 2006). This assemblage dates from the Archean (Spengler et al, 2006; Splengler et al., 2009; Van Roermund, 2009), and the high majoritic component indicates that a minimum pressure of 11.5Gpa at 1800°C (Spengler et al., 2006; Spengler et al., 2009; Van Roermund, 2009). Subsequent recrystallization and re-equilibration produced a rock containing

garnet, orthopyroxene megacrysts with exsolution lamellae of clinopyorxene and possibly Cr-rich spinel, which has been observed only in one sample (Van Roermund, 2009). This assemblage has been interpreted to form at 3-4.5Gpa and 1300-1500°C, as peridotites cooled down from higher Archean to lower Proterozoic geotherms (Carswell and Van Roermund, 2005; Spengler et al., 2006; Van Roermund, 2009).

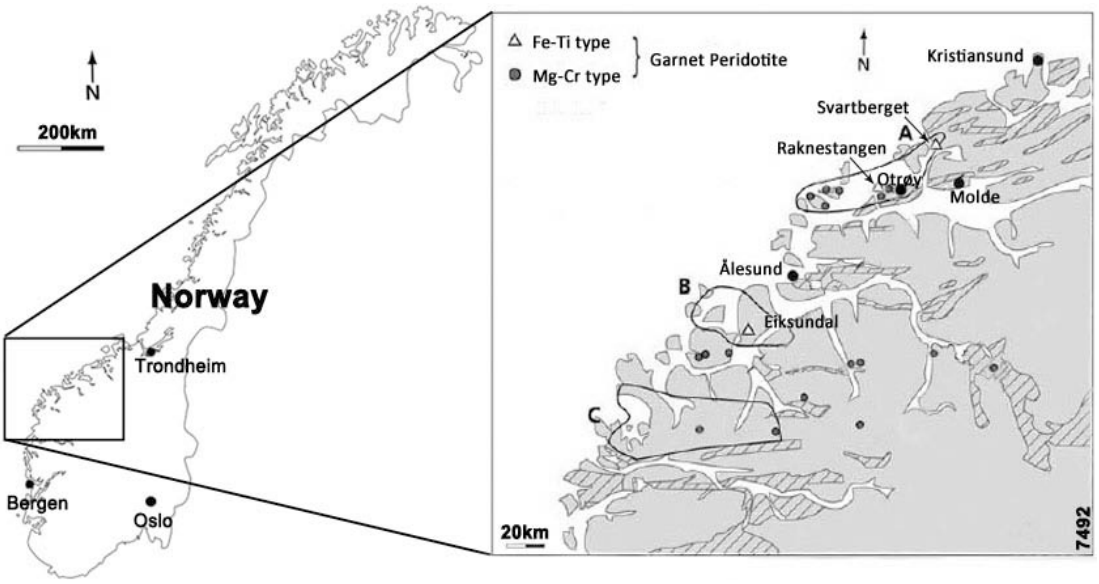

Figure 1. Location maps of the Western Gneiss Region of Norway. A box in the left map (Regional map of Norway) indicates the location of the Western Gneiss Region of Norway, which is magnified on the right. The location of Otrøy Island and the distribution of garnet peridotites (circles and triangles) are indicated in the right map. A, B, and C refer to northern, central, and southern ultra-high pressure domains. Each domain is outlined by black lines. Modified from Van Roermund (2009).

During the Scandian Orogeny, these peridotites (Fig. 1) became incorporated into the subducting Baltican continental crust (Spengler et al., 2006; Van Roermund, 2009). Ongoing subduction of the Baltican crust caused the minerals in the peridotites to undergo the peak metamorphic P-T condition of 5.5-6.5Gpa and 870-920°C (Spengler et

al., 2009). During subsequent uplift and cooling, a neoblastic assemblage, which is characterized by smaller grain size as well as a strong preferred orientation (Spengler et al., 2009), was stabilized. P-T estimates using the core compositions of small grained orthopyroxene (< 0.3mm) and other minerals in this assemblage yield 3.8-4GPa and 820-880°C (Spengler et al., 2009). Continued exhumation produced additional minerals, including matrix amphiboles and an intergrowth of spinel, pyroxenes, and amphibole which surrounds garnet that is commonly referred to as kelyphite (Carswell, 1984; Spengler et al., 2009; Van Roermund, 2009; its Fig. 3). This Scandian overprint is extensively recognized within the northernmost part of the Western Gneiss Region (Cuthbert et al., 2000).

3. ANALYTICAL PROCEDURE

The compositions of the minerals in the samples were analyzed using an electron microprobe located in the Department of Geology at Texas A&M University. Analyses were conducted using an accelerating voltage of 15kV and beam current of 20nA. The beam diameter was 1μm for the analyses of olivine, orthopyroxene, clinopyroxene, garnet, and spinel, and 10μm for the analysis of amphibole.

Olivine and spinel, pyroxene, and garnet analyses were normalized to three, four, and eight cations, respectively. However, amphibole normalization required the quantification of three unknowns: 1) the ratio of Fe^{3+} to Fe^{2+}, 2) oxy/hydroxy content, and 3) vacancies on the crystallographic A-site. Since conventional probe analyses do not provide these values, we used the normalization procedure described in Lamb and Popp (2009). This procedure requires a value of $Fe^{3+}/\Sigma Fe$, where $\Sigma Fe = Fe^{3+} + Fe^{2+}$, and the use of empirically-derived relations between the cation content and the oxy/hydroxyl content of mantle amphibole to determine the amount of oxy/hydroxy components. However, in this study, values of $Fe^{3+}/\Sigma Fe$ were not estimated for amphiboles, and, therefore, amphibole normalization was performed by assuming the minimum ratio of $Fe^{3+}/\Sigma Fe$ that produced a charge-balanced formula. Given this compositional information, a conventional microprobe analysis and a value of $Fe^{3+}/\Sigma Fe$, an iterative approach is used to determine a chemical formula that satisfies the charge balance as well as the constraints on the crystallographic site occupancies (for details, see APPENDIX A).

A redox equilibrium between olivine, orthopyroxene, and spinel was used to determine the values of oxygen fugacities (fO_2) (Wood, 1990). The value of fO_2 estimated from this equilibrium depends strongly upon the value of $Fe^{3+}/\Sigma Fe$ in spinel. Determining the oxidation state of Fe in spinel via balancing the charges of cations versus oxygen using conventional microprobe analyses may result in unfortunately large uncertainties (Wood and Virgo, 1989; Woodland et al., 1991; Canil and O'Neill, 1996). These uncertainties are not entirely random, but they arise from systematic uncertainties in the chemical composition of the standard and/or uncertainties in matrix corrections (Canil and O'Neill, 1996; Wood and Virgo, 1989). However, it is possible to use secondary spinel standards, with known values of $Fe^{3+}/\Sigma Fe$ to correct the values of $Fe^{3+}/\Sigma Fe$ that were originally determined based on charge balance (Wood and Virgo, 1989).

We analyzed the secondary standards of spinels with known $Fe^{3+}/\Sigma Fe$ values of 0.15 to 0.31, as determined by mössbauer spectroscopy (standards provided by Wood, B.). Replicate analyses indicated that charge balance, when applied to these same spinel standards, yielded values of $Fe^{3+}/\Sigma Fe$ that are typically 0.05 to 0.08 larger than the values determined by mössbauer spectroscopy (over the range of $Fe^{3+}/\Sigma Fe = 0.15$ to 0.31). Normalized formulae for the unknown spinels analyzed in this study yielded values of $Fe^{3+}/\Sigma Fe$ from 0.03 to 0.07 based on charge balance. Correcting these values of $Fe^{3+}/\Sigma Fe$ based on the analyses of secondary standards yielded values of $Fe^{3+}/\Sigma Fe$ that were smaller than those based on charge balance and that were, in some cases, approximately equal to 0. However, this correction requires significant extrapolation

from 0.15, the lowest value of $Fe^{3+}/\Sigma Fe$ of our spinel standards, to 0.03. This extrapolation results in a ferric-ferrous correction of dubious accuracy. Thus, in subsequent sections of this paper, we used $Fe^{3+}/\Sigma Fe$ values that were determined via charge balance. We treated these as maximum values because corrections based on the analyses of secondary standards, although uncertain, always yielded smaller values of $Fe^{3+}/\Sigma Fe$ than those estimated using charge balance.

4. MINERALOGY AND MINERAL CHEMISTRY

Four different samples were collected from the Otrøy Island in the Western Gneiss Region of Norway (provided by Drury, M.). All samples consisted of abundant olivines and orthopyroxenes with lesser amounts of coarse-grained garnets, clinopyroxenes, amphiboles, and spinels (Fig. 2). The garnets were surrounded by a fibrous intergrowth of orthopyroxene, clinopyroxene, and spinel with minor amounts of amphibole (kelyphite) (Fig. 3). The retrograde reaction rims of kelyphite were enveloped again by a thin rim of orthopyroxenes and this rim of orthopyroxenes is referred to as 'COR' (Coarse Orthopyroxene Rim) (Obata and Ozawa, 2011). Small nodular spinels were sometimes located between these two reaction rims (Fig. 4). Orthopyroxenes, clinopyroxenes, amphiboles, and spinels occur as matrix phases (Fig. 2), and matrix clinopyroxenes were, in some cases, replaced by amphiboles (Fig. 5).

4.1 Chemical Zoning in Minerals

Microprobe analyses reveal that various minerals in our samples exhibit compositional zoning, consistent with observations reported in previous studies (Medaris Jr, 1984; Carswell, 1986; Spengler et al., 2009; Van Roermund, 2009). Examples of this compositional variation are given in Figures 6 through 13 which plot cations per formula unit against distance across a single mineral grain.

The small size of minerals within the kelyphite made chemical characterization with the electron microprobe challenging. Analyses of mineral grains within the kelyphite were restricted to the grains at least 5μm across in an effort to avoid excitation

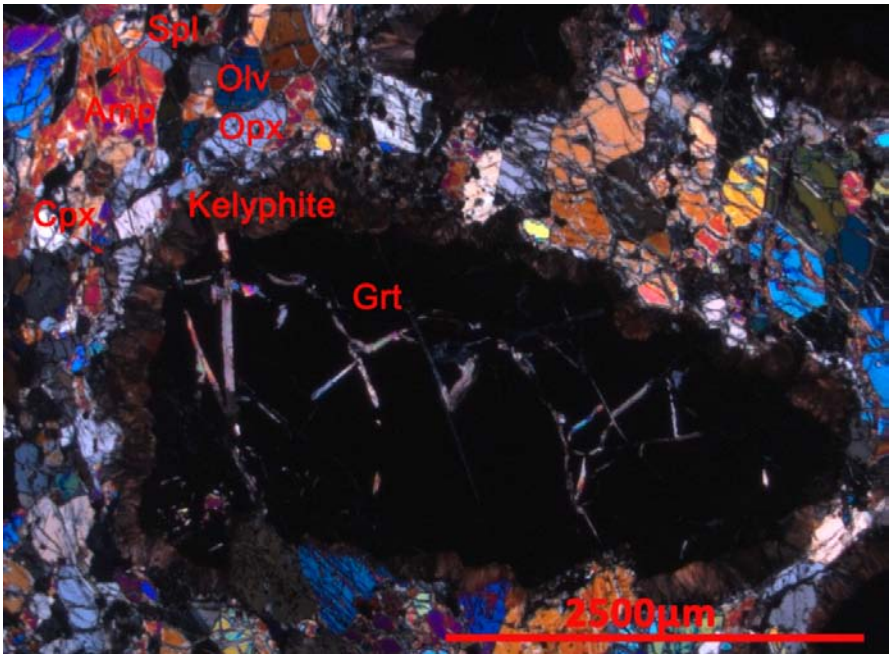

Figure 2. Optical micrograph showing olivines, orthopyroxenes, clinopyroxenes, amphiboles, spinels, and a coarse-grained garnet with a retrograde reaction rim which is an intergrowth of minerals (kelyphite).

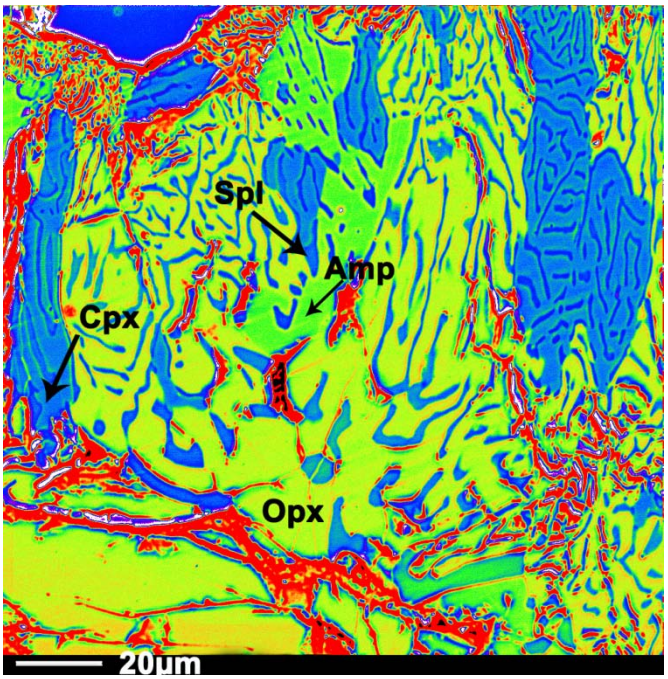

Figure 3. Back-scattered electron image of kelyphite with false color. Note the kelyphite largely consists of orthopyroxene (light green) with large patches of clinopyroxene (light blue), small extent of amphibole (green), and vermicular spinel (dark blue).

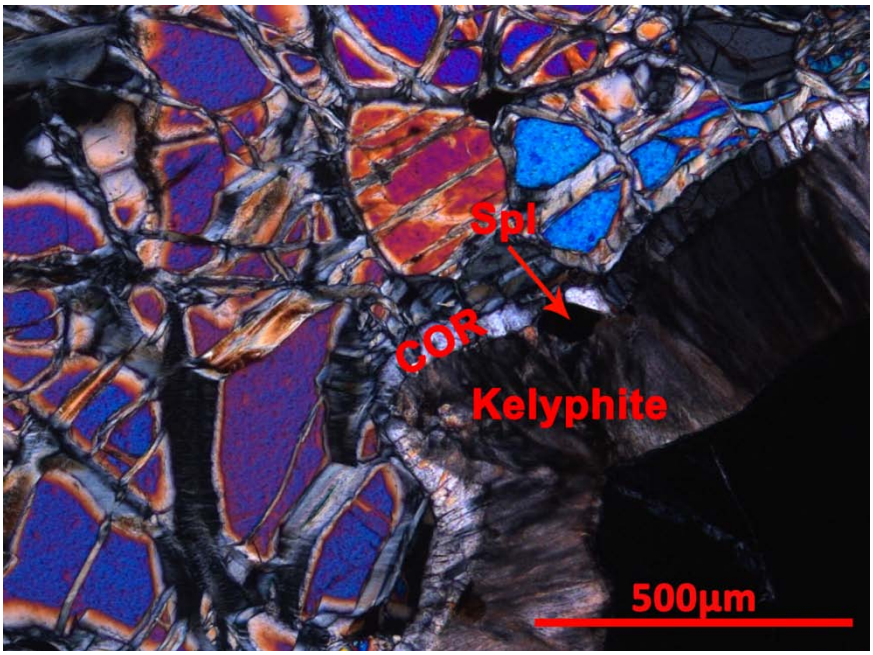

Figure 4. Optical micrograph showing a garnet with a kelyphite rim surrounded by a thin rim of coarse orthopyroxenes (COR). Nodular spinels are intermittently located in between the kelyphite and the coarse orthopyroxene rim.

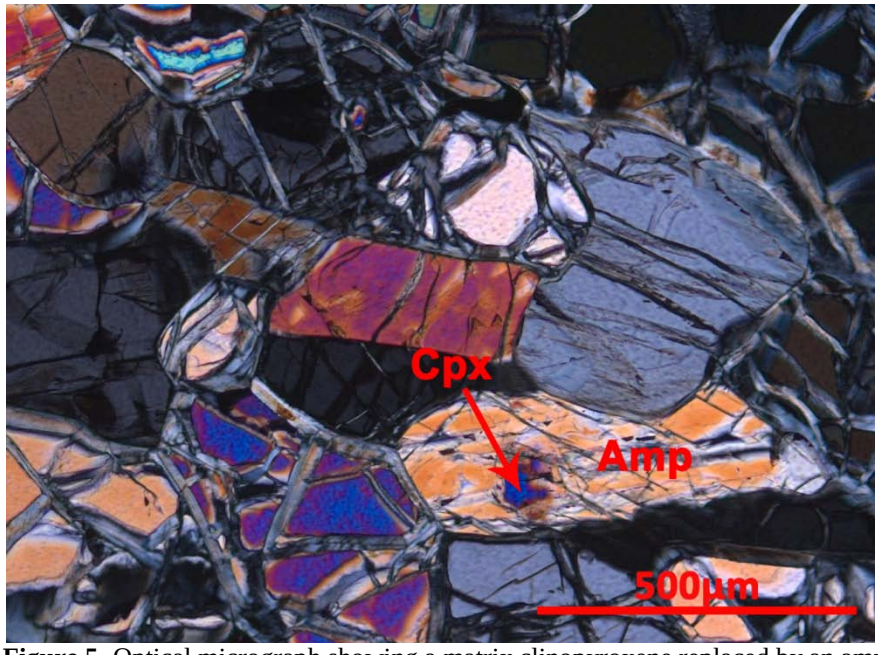

Figure 5. Optical micrograph showing a matrix clinopyroxene replaced by an amphibole.

of x-rays from adjacent minerals. Mineral analyses and normalized outcomes for matrix minerals as well as minerals within the kelyphite are given in APPENDIX B.

4.1.1 Garnet

Garnet in each sample exhibits distinctive compositional zoning (Figs. 6 and 7). Garnet in NUM9a has complex compositional zoning with a relatively homogenous core and more abrupt changes in chemical composition toward the rims (Fig. 6). This garnet, in particular, preserves a relatively large decrease in Cr and coincident increase in Al starting approximately 25μm from the rim. This trend is then reversed with an increase in Cr content and coincident decrease in Al within approximately 15μm from the rim (Fig. 6). These sharp changes in Al and Cr contents occur within a few tens of microns from the rims and are not preserved in other samples. For example, compositional changes are gradual across garnets in NRTP4 and DS0260, but Mg abruptly decreases and Fe sharply increases within the outermost ≈310μm (NRTP4) and ≈140μm (DS0260) of the rims (Fig. 7). Garnet in NRTP4 displays a progressive decrease in Al and a gradual increase in Cr also within ≈310μm of the rim, while garnet in DS0260 shows opposite trends for these elements (Fig. 7). In DS0286, the garnet is relatively homogenous with standard deviation of less than 0.1 for all analyzed oxides (Table 1).

4.1.2 Spinel

Matrix spinels typically exhibit a gradual decrease in Cr and an increase in Al from core to rim (Fig. 8). Spinel inter-growths within the kelyphite rims are rich in Al compared to matrix spinels. For instance, in NRTP4 a single grain of spinel within the

kelyphite contains 57.83wt% Al_2O_3, as compared to the amount of Al_2O_3 in matrix spinels, which ranges from 22.43 to 34.59wt% (see APPENDIX B).

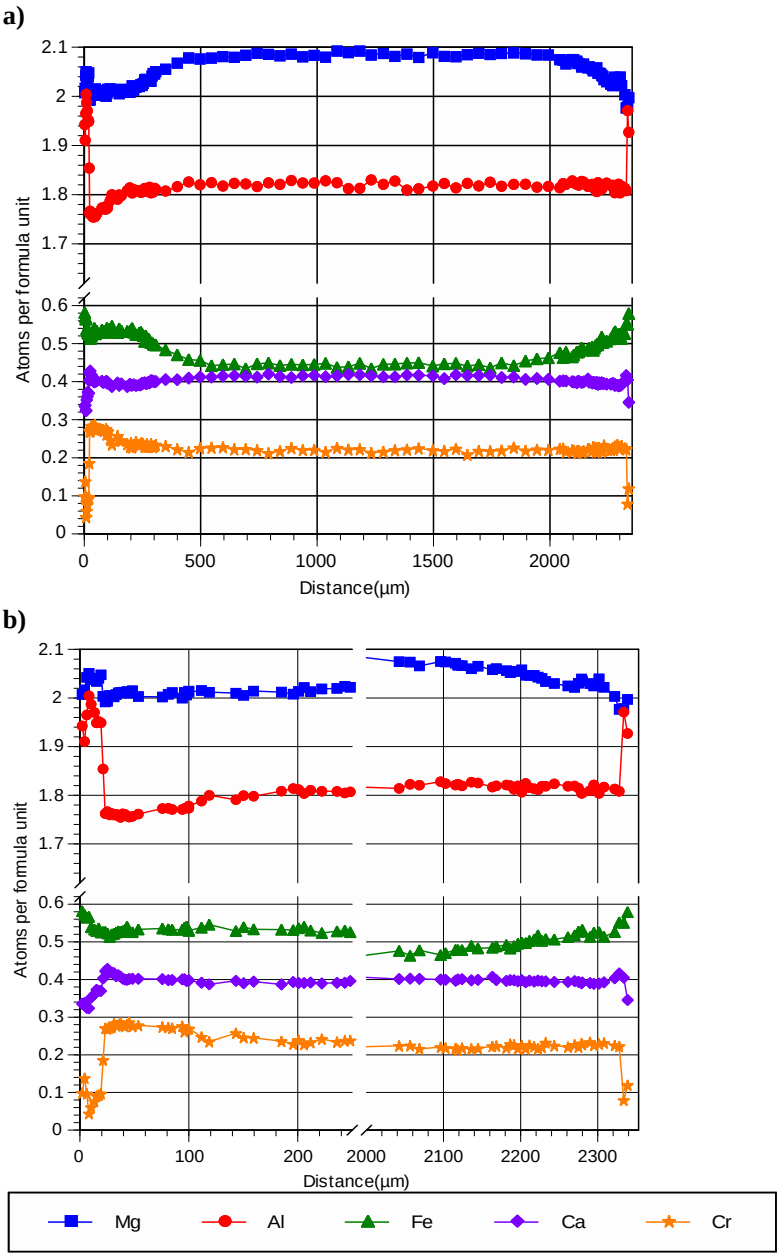

Figure 6. Zoning profiles across garnet in NUM9a without (a) and with (b) a break in the scale along the x-axis. Note a decrease in Cr, probably associated with the spinel formation and a subsequent decrease in Al likely related to the kelyphite-forming reaction.

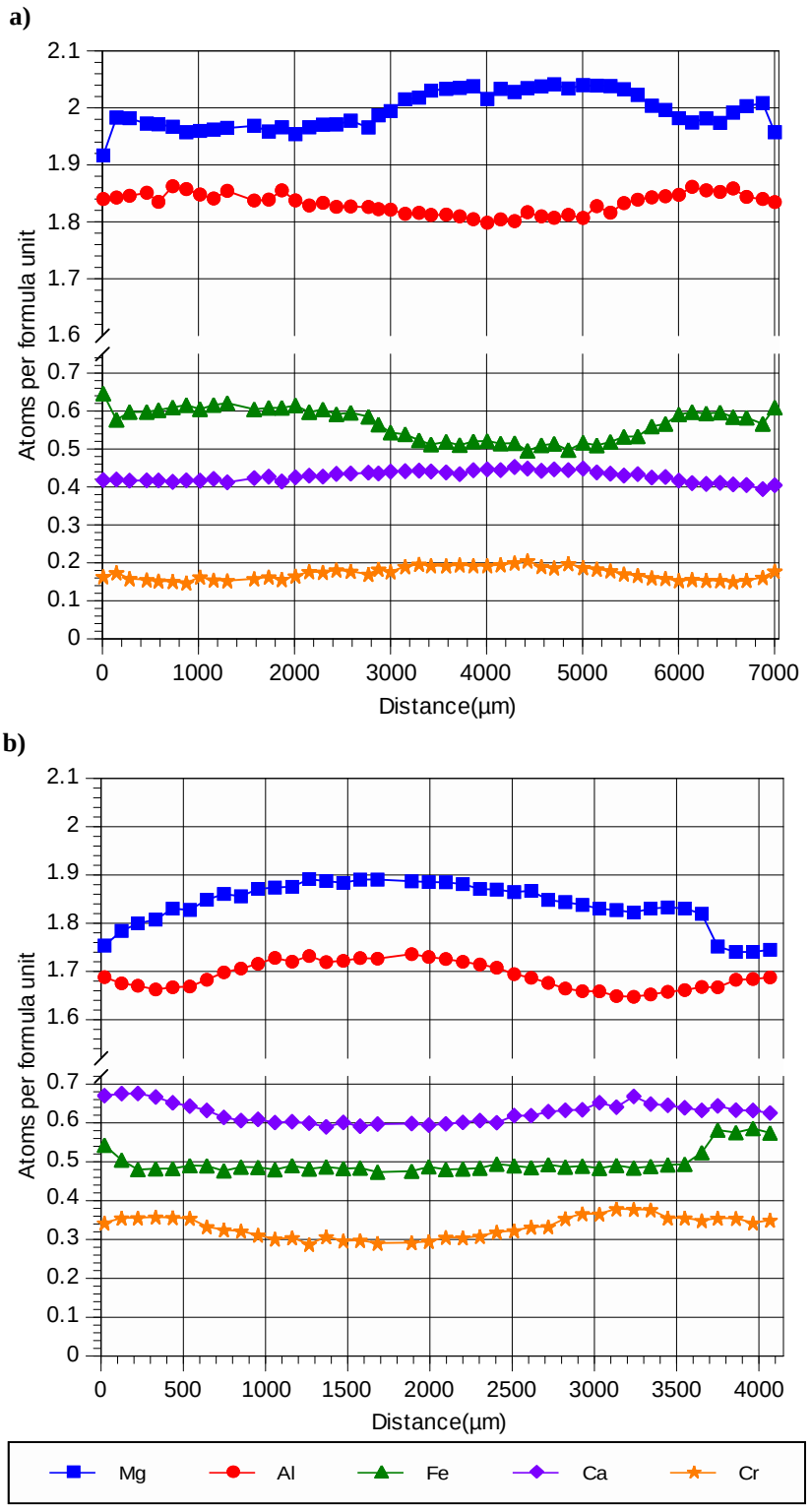

Figure 7. Zoning profiles across garnets. a) NRTP4; b) DS0260. Note a decrease in Cr near rims is small as compared to NUM9a.

Table 1. Microprobe analyses (wt%) of garnet in DS0286 (Distances are from the rim represented by the 1st analysis)

	Rim	717µm	1544µm	1956µm	2505µm	2897µm	3468µm	Rim 4022µm
SiO_2	41.37	41.30	41.25	41.29	41.26	41.57	41.45	41.43
Al_2O_3	22.22	22.15	22.10	22.10	22.09	22.19	22.10	22.05
TiO_2	0.00	0.00	0.00	0.05	0.00	0.00	0.00	0.00
Cr_2O_3	2.81	2.73	2.64	2.78	2.82	2.85	2.86	3.10
FeO	8.97	9.47	9.12	9.59	9.15	9.33	9.34	9.13
MnO	0.52	0.53	0.49	0.45	0.42	0.42	0.47	0.55
MgO	19.19	19.03	18.81	19.13	19.07	19.07	19.09	19.39
CaO	4.97	5.02	4.94	5.06	4.99	5.03	4.91	4.60
Sum	100.04	100.23	99.34	100.43	99.80	100.46	100.22	100.25
Formulae normalized to eight cations								
$Si^{(IV)}$	2.96	2.96	2.98	2.95	2.97	2.97	2.97	2.96
$Al^{(IV)}$	0.04	0.04	0.02	0.05	0.03	0.03	0.03	0.04
$Al^{(VI)}$	1.84	1.83	1.86	1.81	1.84	1.84	1.84	1.82
Ti	0.00	0.00	0.00	0.00	0.00	0.00	0.00	0.00
Cr	0.16	0.16	0.15	0.16	0.16	0.16	0.16	0.18
Fe^{3+}	0.04	0.06	0.01	0.07	0.04	0.03	0.04	0.04
Fe^{2+}	0.50	0.51	0.54	0.50	0.51	0.53	0.53	0.51
Mn	0.03	0.03	0.03	0.03	0.03	0.03	0.03	0.03
Mg	2.05	2.03	2.03	2.04	2.04	2.03	2.04	2.07
Ca	0.38	0.39	0.38	0.39	0.38	0.39	0.38	0.35
Sum	8.00	8.00	8.00	8.00	8.00	8.00	8.00	8.00

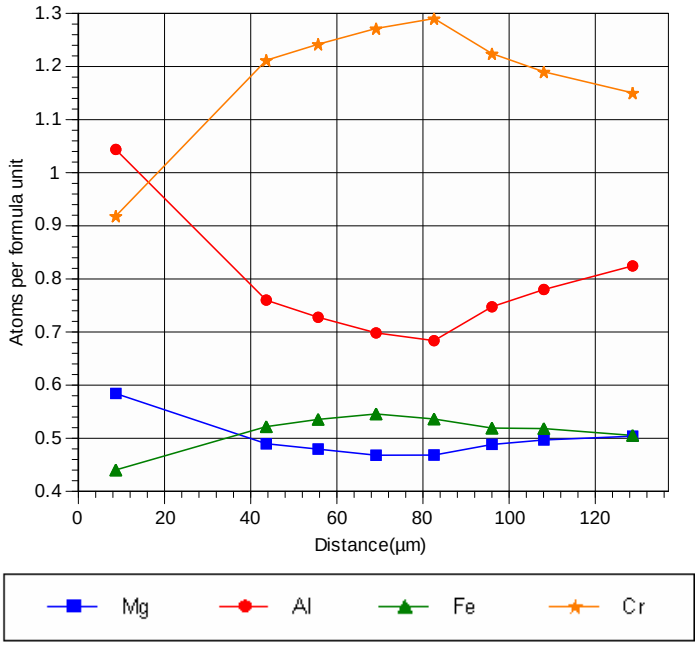

Figure 8. Zoning profiles across matrix spinel in NRTP4.

4.1.3 Orthopyroxene

Matrix orthopyroxenes are characterized by relatively homogenous core compositions with decreasing Mg and increasing Al toward their rims (Fig. 9). A comparison of Al between matrix orthopyroxene and orthopyroxene growing within the kelyphite shows that those within the kelyphite have a much higher Al_2O_3 content (ranging from 2.69 to 10.58wt%; see APPENDIX B) as compared to matrix orthopyroxenes (ranging from 0.28 to 1.86wt%; see APPENDIX B).

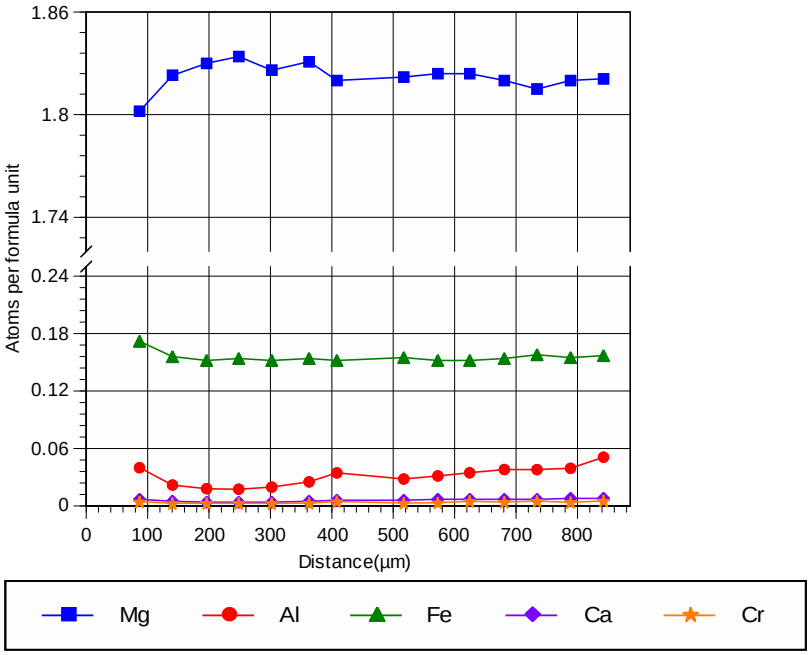

Figure 9. Zoning profiles across matrix orthopyroxene in NRPT4.

The compositions of relatively small grains of orthopyroxenes that surround the kelyphite (COR) change gradually across the entire grains (Fig. 10). The inner part of the COR, adjacent to the kelyphite (Fig. 10; left end), is similar in composition to the

orthopyroxene within the outer part of the kelyphite (Table 2). However, the outer part of the COR, adjacent to the matrix (Fig. 10; right end), has a composition that is similar to the rims of matrix orthopyroxene (Table 2).

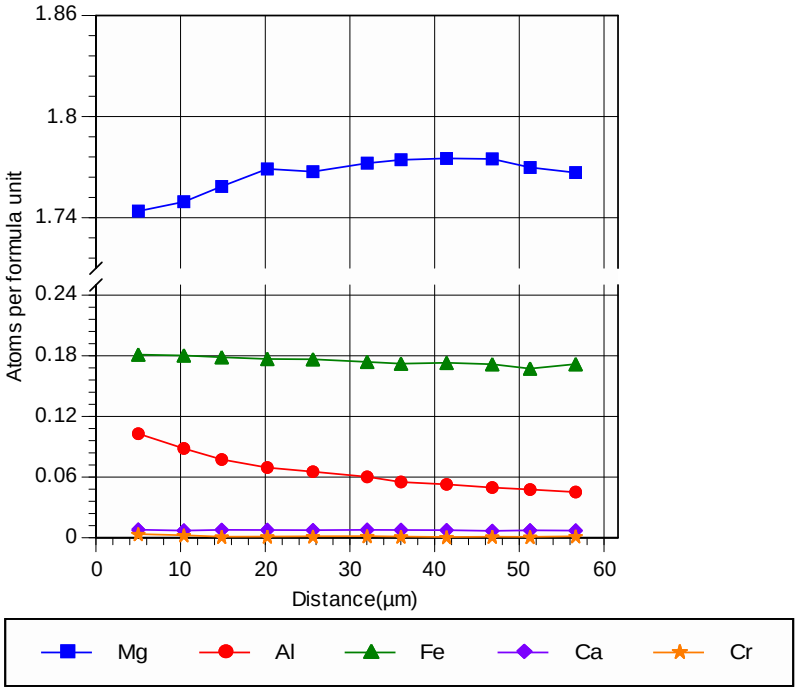

Figure 10. Compositions across an orthopyroxene grain that surrounds kelyphite (COR) in NRTP4. Compositions are plotted from inner (adjacent to the kelyphite) to outer rim (adjacent to the matrix) of COR.

Table 2. Microprobe analyses (wt%) of matrix orthopyroxene, orthopyroxene rim surrounding the kelyphite (COR), and the kelyphite in NRTP4

	Matrix orthopyroxene		**COR**		**Orthopyroxene within kelyphite**	
	Core	**Rim**	**Adjacent to kelyphite**	**Adjacent to the matrix**	**Adjacent to garnet**	**Adjacent to the matrix**
SiO_2	58.53	57.80	56.32	57.36	50.04	56.04
Al_2O_3	0.64	1.00	2.51	1.10	10.58	2.69
TiO_2	0.01	0.00	0.00	0.00	0.00	0.00
Cr_2O_3	0.13	0.17	0.13	0.00	1.11	0.23
FeO	5.41	6.03	6.22	5.89	6.58	6.28

Table 2. Continued

	Matrix orthopyroxene		COR		Orthopyroxene within kelyphite	
	Core	**Rim**	**Adjacent to kelyphite**	**Adjacent to the matrix**	**Adjacent to garnet**	**Adjacent to the matrix**
MnO	0.10	0.19	0.00	0.26	0.21	0.27
MgO	36.15	35.47	33.61	33.99	32.08	33.64
CaO	0.15	0.18	0.22	0.19	0.15	0.21
NiO	0.00	0.00	0.00	0.11	0.00	0.00
Na_2O	0.00	0.00	0.00	0.00	0.00	0.00
K_2O	0.00	0.00	0.00	0.00	0.00	0.00
Sum	101.11	100.83	99.01	98.90	100.74	99.35
Formulae normalized to four cations						
Si $^{(IV)}$	1.98	1.97	1.96	2.00	1.71	1.95
Al $^{(IV)}$	0.02	0.03	0.04	0.00	0.29	0.06
Al $^{(VI)}$	0.01	0.01	0.06	0.05	0.14	0.06
Ti	0.00	0.00	0.00	0.00	0.00	0.00
Cr	0.00	0.00	0.00	0.00	0.03	0.01
Fe^{3+}	0.01	0.02	0.00	0.00	0.12	0.00
Fe^{2+}	0.15	0.16	0.18	0.17	0.06	0.18
Mn	0.00	0.01	0.00	0.01	0.01	0.01
Mg	1.83	1.80	1.74	1.77	1.63	1.74
Ca	0.01	0.01	0.01	0.01	0.01	0.01
Ni	0.00	0.00	0.00	0.00	0.00	0.00
Na	0.00	0.00	0.00	0.00	0.00	0.00
Sum	4.00	4.00	4.00	4.00	4.00	4.00

4.1.4 Clinopyroxene

Matrix clinopyroxenes are compositionally zoned with increasing Ca and Mg and decreasing Na and Al toward the rims (Fig. 11). However, these compositional variations are greater in clinopyroxene grains from NUM9a and NRTP4 (Fig. 11). Clinopyroxenes that are partially replaced by amphibole are compositionally homogenous (Fig. 12).

Clinopyroxene within the kelyphite typically has higher Al_2O_3 contents (ranging from 2.24 to 5.66wt%; see APPENDIX B) as compared to matrix clinopyroxene (ranging from 0.96 to 2.91wt%; see APPENDIX B).

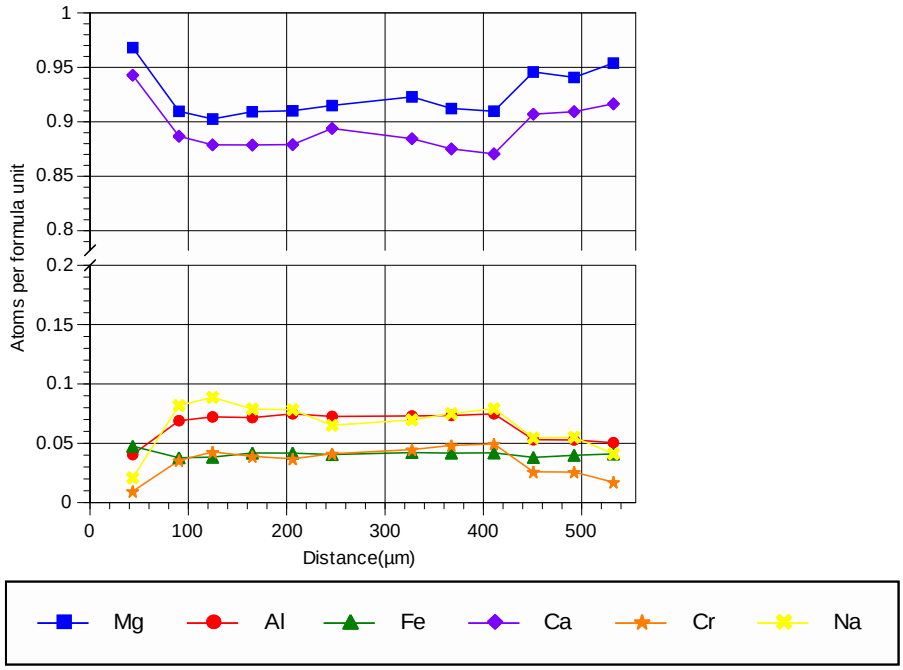

Figure 11. Zoning profiles across matrix clinopyroxene in NRPT4 with no evidence of amphibole replacement.

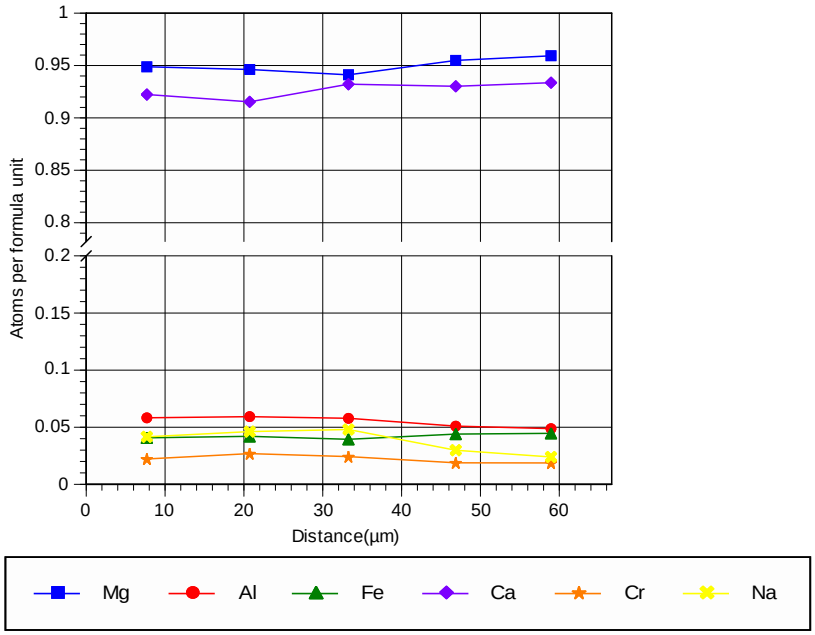

Figure 12. Compositions across matrix clinopyroxene replaced by amphibole in NRTP4. Note the rim compositions of un-replaced clinopyroxene (Fig. 11) are close to the overall compositions of clinopyroxene replaced by amphibole.

4.1.5 Amphibole

Matrix amphiboles in our samples (Table 3) are relatively homogenous including those that partically replace matrix clinopyroxene (Table 4). Matrix amphiboles in the proximity of the kelyphite, however, show slight compositional zoning especially toward those rims in relatively close proximity to the kelyphite (Table 3; Fig.13a; right end).

Table 3. Microprobe analyses (wt%) of matrix amphibole in close proximity to kelyphite in NRTP4 (Rim* is adjacent to the matrix, distance from Rim* are given for subsequent analyses, and Rim** is adjacent to kelyphite)

	Rim*	**98µm**	**661µm**	**907µm**	**1048µm**	**Rim****
SiO_2	45.46	45.81	46.23	45.23	44.93	45.17
Al_2O_3	13.59	13.29	12.89	13.09	13.86	14.79
TiO_2	0.30	0.37	0.35	0.28	0.36	0.14
Cr_2O_3	1.98	2.12	2.15	2.30	1.98	1.47
FeO	2.34	2.35	2.33	2.86	2.94	2.73
MnO	0.00	0.00	0.00	0.00	0.00	0.00
MgO	18.48	18.83	18.76	18.59	18.69	17.51
CaO	12.39	12.34	12.33	11.89	11.94	12.31
NiO	0.00	0.00	0.00	0.00	0.00	0.00
Na_2O	2.53	2.37	2.36	2.28	2.32	2.23
K_2O	0.06	0.12	0.09	0.08	0.00	0.00
SUM	97.13	97.59	97.49	96.60	97.02	96.35

Table 4. Microprobe analyses (wt%) of matrix amphibole replacing matrix clinopyroxene in NRTP4 (Distances are from the rim adjacent to the 1st analysis)

	Rim	**127µm**	**250µm**	**394µm**	**Rim 532µm**
SiO_2	46.12	45.27	45.92	45.57	45.89
Al_2O_3	12.97	11.86	12.95	12.90	12.92
TiO_2	0.38	0.31	0.36	0.35	0.34
Cr_2O_3	1.96	2.06	2.04	2.12	1.95
FeO	2.58	3.28	2.28	2.40	2.56
MnO	0.00	0.00	0.00	0.00	0.00
MgO	19.60	20.47	19.48	19.48	19.74
CaO	12.57	11.31	12.45	12.34	12.22
NiO	0.00	0.00	0.00	0.00	0.00
Na_2O	2.68	2.43	2.55	2.65	2.65
K_2O	0.08	0.07	0.20	0.16	0.07
SUM	98.94	97.05	98.24	97.97	98.33

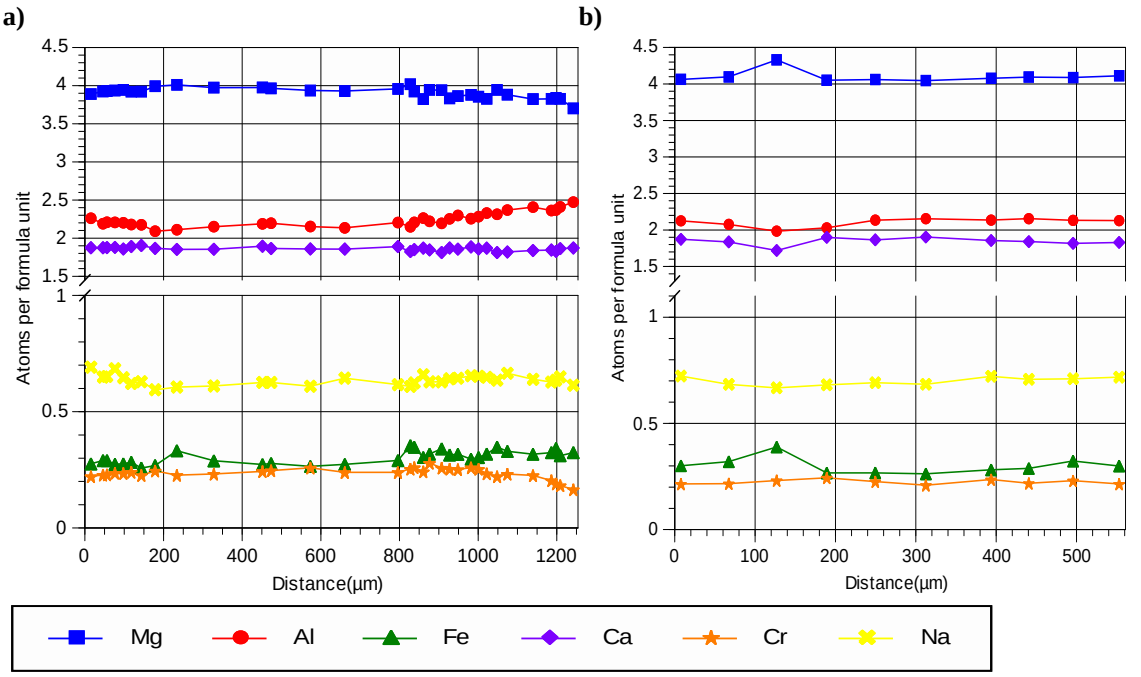

Figure 13. Zoning profiles across matrix amphiboles in NRTP4. a) Compositions of matrix amphibole; the right rim of this amphibole is close to the kelyphite relative to its left rim. b) Compositions of matrix amphibole which texturally replaces matrix clinopyroxene.

Amphibole forming within the kelyphite has higher Al_2O_3 content (ranging from 14.64 to 15.94 wt%; see APPENDIX B) than matrix amphibole. Its composition is similar to the rim of matrix amphibole in close proximity to the kelyphite (Table 5; Fig. 13a; right end).

Table 5. Microprobe analyses (wt%) of matrix amphibole and fine-grained amphiboles within the kelyphite from NRTP4

	Matrix amphibole		**Amphibole within the kelyphite**	
	Core	**Rim (Adjacent to kelyphite)**	**Adjacent to garnet**	**Adjacent to the matrix**
SiO_2	45.35	45.17	44.61	44.54
Al_2O_3	13.15	14.79	14.64	14.71
TiO_2	0.39	0.14	0.28	0.28
Cr_2O_3	2.18	1.47	1.89	2.09

Table 5. Continued

	Matrix amphibole		Amphibole within the kelyphite	
	Core	**Rim (Adjacent to kelyphite)**	**Adjacent to garnet**	**Adjacent to the matrix**
FeO	2.31	2.73	2.92	2.83
MnO	0.00	0.00	0.07	0.06
MgO	18.89	17.51	18.34	18.18
CaO	12.52	12.31	12.50	12.43
NiO	0.00	0.00	0.05	0.09
Na_2O	2.29	2.23	2.24	2.37
K_2O	0.29	0.00	0.05	0.03
Sum	97.35	96.35	97.57	97.61
Normalized formulae				
$Si^{(IV)}$	6.41	6.41	6.29	6.28
$Al^{(IV)}$	1.59	1.59	1.71	1.72
$Ti^{(M123)}$	0.04	0.02	0.03	0.03
$Al^{(M123)}$	0.60	0.88	0.72	0.73
$Cr^{(M123)}$	0.25	0.17	0.21	0.23
$Fe^{3+(M123)}$	0.00	0.00	0.00	0.00
$Fe^{2+(M123)}$	0.14	0.24	0.18	0.18
$Mg^{(M123)}$	3.97	3.70	3.85	3.82
$Mn^{(M123)}$	0.00	0.00	0.00	0.00
$Ni^{(M123)}$	0.00	0.00	0.01	0.01
$Mg^{(M4)}$	0.00	0.00	0.00	0.00
$Fe^{2+(M4)}$	0.13	0.09	0.17	0.15
$Mn^{(M4)}$	0.00	0.00	0.01	0.01
$Ca^{(M4)}$	1.87	1.87	1.83	1.84
$Na^{(M4)}$	0.00	0.04	0.00	0.00
$Ca^{(A)}$	0.01	0.00	0.06	0.04
$Na^{(A)}$	0.63	0.57	0.61	0.65
$K^{(A)}$	0.06	0.00	0.01	0.01
Vac	0.31	0.43	0.32	0.31
F	0.00	0.00	0.00	0.00
Cl	0.00	0.00	0.00	0.00
O	0.04	0.02	0.03	0.03
OH	1.96	1.99	1.97	1.97

4.2. Interpretation of Zoning Profiles of Minerals

Garnet-bearing peridotites in the Western Gneiss Region of Norway have a protracted history which includes UHP metamorphism and subsequent uplift from a depth of approximately 200km (Medaris Jr, 1984; Carswell, 1986; Spengler et al., 2009;

Van Roermund, 2009). This history is recorded by a sequence of mineral assemblages and/or compositional zoning within individual minerals that had been produced through time (Medaris Jr, 1984; Carswell, 1986; Spengler et al., 2009; Van Roermund, 2009). We used mineral equilibria to estimate the values of P-T and water activities (aH_2O), and therefore, it was critical to determine the chemistry, within compositionally zoned minerals, that represents equilibrium with amphibole.

Fine grained olivine, orthopyroxene, clinopyroxene, and spinel in the matrix are texturally consistent with the neoblastic assemblage which was formed during the Baltican subduction related to the Scandian Orogeny (Fig. 2). Matrix orthopyroxenes preserve an Al-low core with an increase in Al near rims (Fig. 9). These compositional trends are similar to those of orthopyroxene grains that were interpreted to re-crystallize during Scandian subduction (Carswell, 1984; Spengler et al., 2009). Spengler et al. (2009) described the increase in Al near rims of orthopyroxene as reflecting re-equilibration during exhumation stages.

Partial replacement of matrix clinopyroxene by amphibole (Fig. 5) suggests that matrix amphibole post-dates clinopyroxene. This partially replaced matrix clinopyroxene is similar in compositions to the rim of matrix clinopyroxene with no evidence of amphibole replacement (Figs. 11 and 12). Thus, the rim compositions of the matrix clinopyroxene likely equilibrated with amphibole.

The textural similarity between matrix orthopyroxene and clinopyroxene (Fig. 2) suggests they shared the same evolutionary history. This, combined with their close proximity indicates that rim compositions of two pyroxenes likely reflect equilibration

during uplift. A similar argument can be made for matrix spinels, as they share proximity and textural similarity with matrix pyroxenes. Thus, given our previous argument that amphiboles are in equilibrium with clinopyroxene rims, estimates of aH_2O that are based on amphibole equilibria should be made using rim compositions of pyroxenes and spinels.

Certain garnets preserve internal changes in composition that are relatively large and these changes occur in the outermost portions of a grain. Garnet in NUM9a, for example, exhibits a sudden drop in Cr coincident with an increase in Al within 25μm of the rim (Fig. 6). This trend is reversed with a drop in Al and increase in Cr as the distance to the rim decreases (Fig. 6). Spinel forms at the expense of garnet as pressures decrease, and Cr is preferentially partitioned into spinel relative to garnet (Green and Ringwood, 1970; Klemme, 2004; its Fig. 1; Grütter et al., 2006). This suggests that the formation of spinel will result in a decrease in the Cr content of the garnet. If so, the compositions of the garnet with the lowest Cr content would correspond to the rim compositions of matrix spinel and, thus, best represent the equilibrium with amphibole.

Kelyphite replaces garnet, and its formation may produce compositional changes near the rims of garnet. Mineral constituents within the kelyphite are significantly richer in Al than the same minerals in the matrix (see previous description). Therefore, the formation of kelyphite may account for the sharp decrease in Al and concomitant increase in Cr that occur within 15μm of the rim in the garnet of NUM9a (Fig. 6).

Kelyphite replaces the outermost portions of garnets. Consequently, any compositional variation developed prior to kelyphite formation that was originally

preserved in the outer rims of a garnet may be lost if this portion of the garnet is consumed by the kelyphite forming reaction. This may explain why garnets with well-developed kelyphite rims have little internal compositional variation (e.g., Fig. 7), as opposed to garnets with small or non-existent kelyphite rims (e.g., Fig. 6). In some cases the thickness of the kelyphite rims may vary along the circumference of a single garnet. For instance, traverse 1 and 2 (Fig. 14) show the locations of two series of analyses that are approximately perpendicular to the rim of a garnet in sample NUM9a. The electron microprobe analyses performed along traverse 1 include compositions from a portion of the garnet rim with little or no adjacent kelyphite. This portion of the garnet exhibits

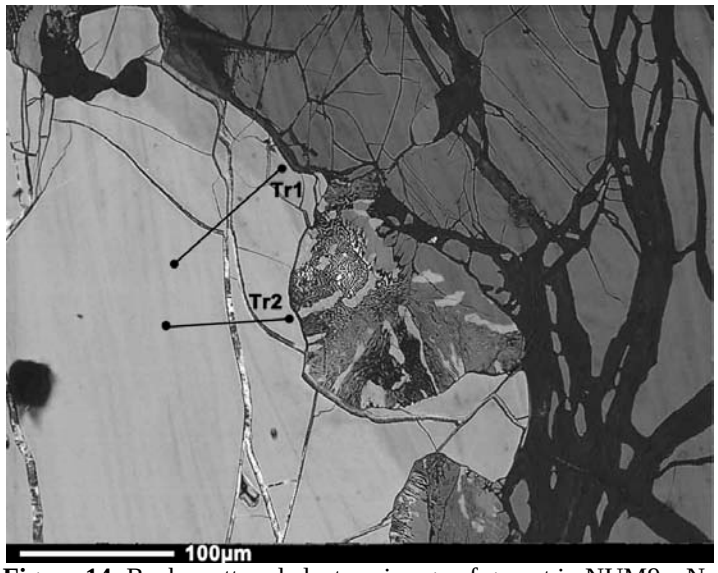

Figure 14. Back-scattered electron image of garnet in NUM9a. Note traverse 2(Tr2) is adjacent to relatively well-grown kelyphite as compared to traverse 1(Tr1).

relatively large changes in composition, as the outermost portion of this garnet preserves a decrease in Cr with a coincident increase in Al, which is followed by an increase in Cr

and a simultaneous decrease in Al from core to rim (Fig. 15a). The chemical composition of the same garnet along traverse 2 (Fig. 14), which is adjacent to well-developed kelyphite, exhibits relatively little change in composition toward the rim (Fig. 15b). This correlation between the development of kelyphite and the general lack of core-to-rim chemical variation is consistent with the idea that the original rim of the garnet was consumed by the kelyphite forming reaction and this resulted in the loss of the strongly zoned portions of this mineral.

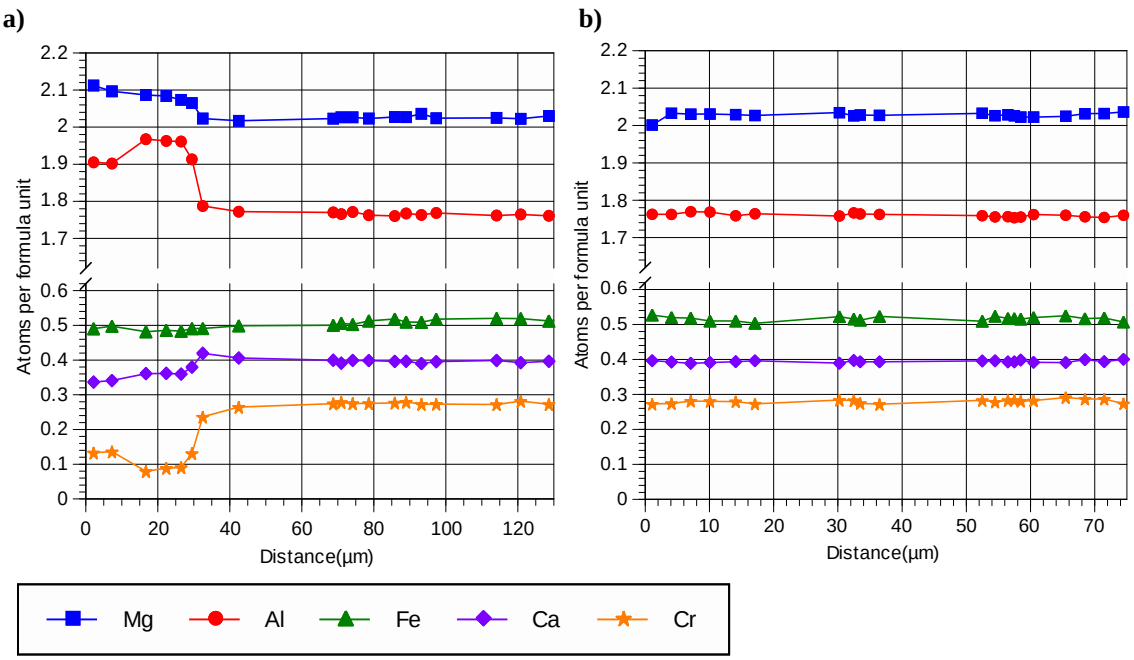

Figure 15. Zoning profiles across the garnet in NUM9a. a) Traverse 1; b) Traverse 2. Note a decrease in Cr near rim is distinctive within Traverse 1.

Compositional similarities between the rim of matrix amphibole in close proximity to the kelyphite and amphibole within the kelyphite suggest that these

minerals approached equilibrium (Table 5). However, most matrix amphibole compositions differ slightly from the compositions of amphibole in the kelyphite, suggesting that some amphibole was present prior to kelyphite formation. If the abrupt decrease in the Al content of the garnet relates to kelyphite formation then the matrix amphibole may have formed prior to this decrease in Al content of garnet preserved in certain garnets (Fig. 6).

This loss of compositional zoning by the extensive growth of kelyphite is also obviously observed when comparing variations in compositions of garnets in different samples, each of which develops a different degree of kelyphite formation. The garnet in sample NUM9a, for example has a relatively thin kelyphite rim and the outermost portion of this garnet preserves a sharp changes in Cr and Al contents as described previously (Fig. 6). In NRTP4, the kelyphite rim is larger than that in sample NUM9a, and the zoning profiles of the garnet in this sample do not exhibit the same abrupt changes in composition near the rims of this mineral as compared to the garnet in NUM9a. Relatively large changes in composition, similar to those found within 40μm of the rim of garnets in NUM9a, may have once existed near garnet rims in NRTP4, however, this portion of the garnet may have been consumed to produce kelyphite. Garnet within NRTP4 does exhibit a gradual decrease in Cr followed by its increase, which are coincident with a progressive increase and then a decrease in Al toward the rims (Fig. 7a). This change in composition is consistent with spinel formation, which would explain the decrease in Cr-content, followed by the development of Al-rich kelyphite. Thus, even though the compositional shifts in Cr and Al are gradual, we

interpret the lowest Cr portion of the garnet rim as having equilibrated with the rim of the spinel which, in turn likely equilibrated with the rims of other matrix phases, such as amphibole.

Garnets from DS0260 and DS0286, were more homogeneous with no well-defined minimum Cr-content near the rims. However, the subtle decline in Cr-content may still be a sign of spinel formation. Furthermore, change in the amounts of other cation, such as Mg, also indicates mineral growth likely related to the development of matrix phases. Thus, the compositions of the outermost rims of the garnet in these two samples (Fig. 7b) are considered to be in equilibrium with the rims of other matrix phases, including amphibole.

Olivines in all samples do not display any significant compositional zoning, and thus, the average of the compositions was used to determine the activity of olivine in equilibrium with amphiboles.

5. PRESSURE AND TEMPERATURE ESTIMATES

Estimating aH_2O based on amphibole equilibria requires estimates of the P and T of mineral equilibration. Various geothermobarometers are available for estimating the pressure and temperature conditions of garnet-bearing peridotites (O'Neill and Wood, 1979; O'Neill, 1980; Brey and Kohler, 1990; Taylor, 1998; Nimis and Taylor, 2000; Wu and Zhao, 2007; Nimis and Grütter, 2010). Among the widely-used thermometers, Taylor's formulation of the two-pyroxene thermometer effectively reproduces experimental temperatures over wide ranges of composition and pressure (Taylor, 1998; Nimis and Grütter, 2010). According to Nimis and Grütter (2010), this formulation also agrees with Brey and Kohler's Ca-in-orthopyroxene thermometer as modified by Nimis and Grütter (2010) to within ±90˚C and with the orthopyroxene-garnet thermometer (Nimis and Grütter, 2010) to within ±70˚C. Based on these observations, we used Taylor's two-pyroxene thermometer in conjunction with the selected rim compositions of minerals to estimate the temperature of mineral equilibration for each sample. The estimated condition was compared to the conditions obtained from two other thermometers, i.e., the modified Ca-in-orthopyroxene thermometer and the orthopyroxene-garnet thermometer, as suggested by Nimis and Grütter (2010).

We used an Al-in-orthopyroxene barometer that was formulated by Nickel and Green (1985) to estimate pressures. The reliability of their barometer has been supported by its ability to reproduce experimental pressures and by the consistency of estimated results with local geotherms (Nimis and Grütter, 2010; Grütter, 2009).

Results of P and T are given in Table 6. Temperatures estimated from Taylor's two pyroxene thermometer range from 700 to 780˚C. The temperature estimate for each sample is consistent, within the uncertainties mentioned above, with temperature estimates based on the Nimis and Grutter and the modified Brey and Kohler thermometers. This indicates that these thermometers yield reliable estimates for the temperature of mineral equilibration for each sample. Pressure ranges from 17 to 27kbar.

Pressures and temperatures estimated in this study are similar to the conditions inferred during exhumation of the orogenic peridotites in the Otrøy Island as well as adjacent Flemsøy and Moldefjord as determined by Spengler et al., (2009) (Fig. 16).

Table 6. Pressure and temperature estimates based on three different combinations of geothermometers in conjunction with the geobarometer of Nickel and Green (1985)

Sample	**Taylor(98)** (˚C **& kbar)**	**Corrected Brey and Köhler(09)** (˚C **& kbar)**	**Nimis and Grutter(09)** (˚C **& kbar)**
NRTP4	720, 24	660, 21	670, 21
DS0260	780, 27	690, 24	810, 28
DS0286	700, 17	680, 16	770, 20
NUM9a	740, 27	650, 22	670, 23

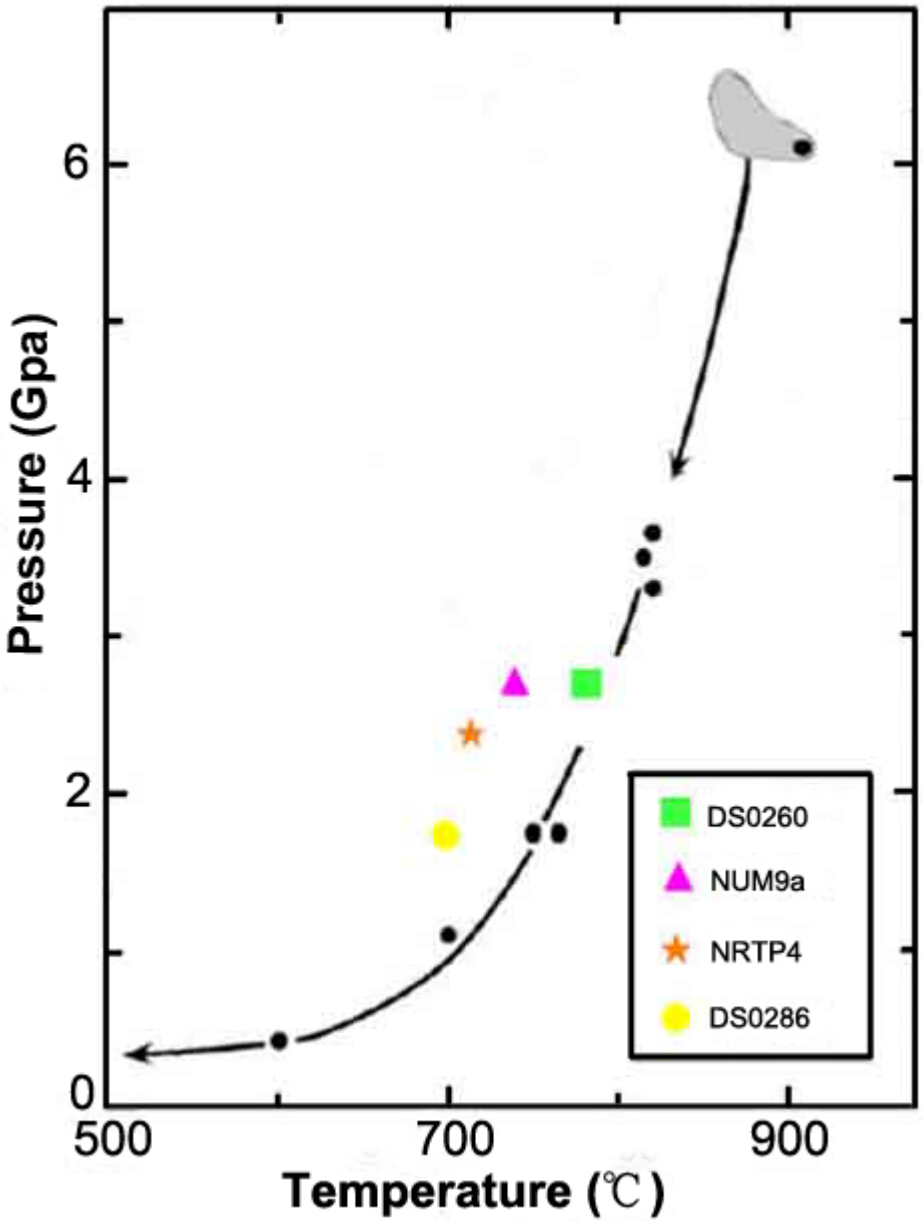

Figure 16. P-T diagram showing P-T estimates derived from orogenic peridotite in the Otrøy Island as well as adjacent Flemsøy and Moldefjord (Modified from Spengler et al., 2009). The large gray area indicates the estimates from Otrøy and Flemsøy, and filled circles indicate the estimates from Moldefjord. P-T estimates determined from the samples of this study are plotted together as points. Note our P-T estimates are in reasonable agreement with the exhumation path of Spengler et al. (2009).

6. ESTIMATING H_2O ACTIVITIES USING AMPHIBOLE DEHYDRATION EQUILIBRIA

H_2O activities in this study were estimated by the following amphibole dehydration equilibria:

$$\mathrm{En} + 2\mathrm{Parg} = 4\mathrm{Di} + 2\mathrm{Jd} + 2\mathrm{Fo} + 2\mathrm{Sp} + \mathrm{H_2O} \quad (1)$$

where En is enstatite, Parg is pargasite, Di is diopside, Jd is jadeite, Fo is forsterite, and Sp is spinel. We chose this particular equilibrium because the amphiboles in the samples of this study are pargasite rich. Determining values of aH_2O from the equilibrium of (1) requires the determination of the activities of all mineral end members in natural phases. The equilibrium constant for this equilibrium is given by:

$$K_{eq} = \frac{(a_{CaMgSi2O6}^{clinopyroxene})^4 \cdot (a_{NaAlSi2O6}^{clinopyroxene})^2 \cdot (a_{Mg2SiO4}^{olivine})^2 \cdot (a_{MgAl2O4}^{spinel})^2 \cdot a_{H_2O}}{(a_{Mg2Si2O6}^{orthopyroxene}) \cdot (a_{NaCa2Mg4Al3Si6O22(OH)2}^{amphibole})^2} \quad (2)$$

Thus, the following end members were considered: Mg_2SiO_4 (forsterite) in olivine, $Mg_2Si_2O_6$ (enstatite) in orthopyroxene, $CaMgSi_2O_6$ (diopside) in clinopyroxene, $NaAlSi_2O_6$ (jadeite) in clinopyroxene, $MgAl_2O_4$ (spinel) in spinel, and $NaCa_2Mg_4Al_3Si_6O_{22}(OH)_2$ (pargasite) in amphibole.

As discussed previously, the chemical composition of pargasite was normalized to yield the maximum OH content in Z-site. This would maximize the value of $a_{NaCa2Mg4Al3Si6O22(OH)2}^{amphibole}$ and the calculation based on the equilibrium of (1) would yield the maximum estimate of aH_2O given the values of end member activities of minerals. We used the MELTS software package to estimate the end-member activities of

forsterite, enstatite, diopside, jadeite, and spinel because these a-X models were developed specifically for mantle pressures, temperatures, and compositions (Table 7; Asimow and Ghiorso, 1998; Ghiorso and Sack, 1995). However, the end-member activities of pargasites were estimated via the a-X model developed by Dale et al. (2005), even though their model is consistent with the dataset developed for the use of THERMOCALC software (see the discussion in Lamb and Popp, 2009). This decision was made because Dale et al.'s a-X model is a well-calibrated thermodynamic model based on a relatively extensive compositional system of Na_2O-CaO-FeO-MgO-Al_2O_3-SiO_2-H_2O-O (NCFMASHO). Furthermore, the model uses a dataset based on the solvus of naturally-occurring amphibole pairs, which makes it sensitive to the thermodynamics of co-existing phases (Dale et al., 2005). These factors indicate that this model will yield accurate a-X estimates, particularly for the pargasite component, as compared to amphibole model developed for MELTS, since it is based on the relatively simple Ca-Mg-Fe^{2+} quadrilateral system (Ghiorso and Evans, 2002). The estimated activities of pargasites were corrected in order to consider the solid solution between OH and O^{2-} in the Z site (Table 7; Lamb and Popp, 2009).

Lamb and Popp (2009) showed that there was often good agreement between the activities of various end-members, such as forsterite in olivine and diopside in clinopyroxene, as estimated from the a-X model of MELTS and the various models of THERMOCALC, even though the two programs are based on different datasets. These similarities suggest that THERMOCALC can be used in conjunction with activity models based on MELTS to estimate aH_2O for mantle conditions (Lamb and Popp,

2009). Therefore, THERMOCALC software was used to locate the dehydration reaction of (1) as a function of temperature, pressure, and aH_2O (Fig. 17). Values of aH_2O for all samples range from 0.12 to 0.36. This may suggest that samples were consistent in respect to the amounts of H_2O (Table 8).

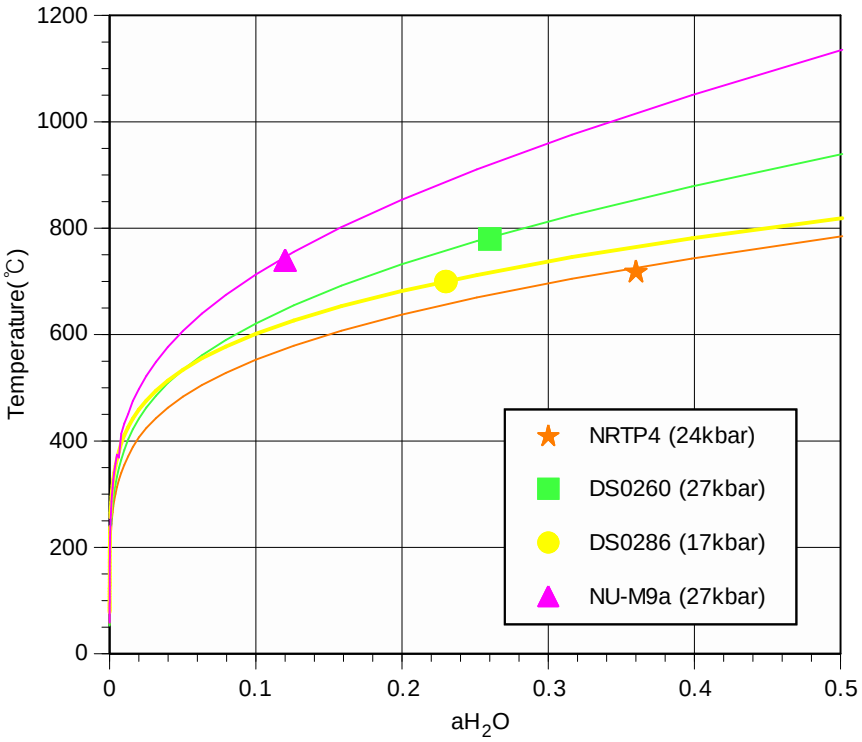

Figure 17. Amphibole dehydration curve plotted as a function of temperatures and water activities at an equilibrium pressure for each sample. The activity of H_2O estimated from amphibole dehydration equilibrium for each sample is also plotted as a point along the corresponding curve.

Table 7. Activities of mineral end members in natural phases

	NRTP4	**DS0260**	**DS0286**	**NUM9a**
Enstatite	0.85	0.84	0.85	0.88
Diopside	0.91	0.88	0.90	0.85
Jadeite	0.01	0.04	0.01	0.07
Forsterite	0.85	0.83	0.85	0.87
Spinel	0.49	0.45	0.51	0.46
Pargasite	0.36	0.52	0.47	0.53

Table 8. H_2O activities estimated from amphibole dehydration equilibrium

Sample	aH_2O (Dehydration)
NRTP4	0.36
DS0260	0.26
DS0286	0.23
NUM9a	0.12

7. OXYGEN FUGACITY ESTIMATES

The oxygen fugacity (fO_2) of each sample was estimated relative to that of fayalite-magnetite-quartz (FMQ) redox buffer using the following redox equilibria:

$$6Fe_2SiO_4(\text{olivine}) + O_2 = 3Fe_2Si_2O_6(\text{orthopyroxene}) + 2Fe_3O_4(\text{spinel}) \quad (3)$$

We chose to use the Wood version of this oxybarometer (Wood, 1990), which is given by:

$$\Delta\log(fO_2)^{FMQ} = 0.35 + \frac{220}{T(K)} - \frac{0.0369P(bars)}{T(K)} - 12\log\left(X_{Fe}^{olv}\right) - \frac{2620(X_{Mg}^{olv})^2}{T(K)} + 3\log\left(X_{Fe}^{M1}X_{Fe}^{M2}\right)^{opx} + 2\log\left(a_{Fe_3O_4}^{sp}\right) \quad (4)$$

where X_{Fe}^{olv}, X_{Mg}^{olv} are the mole fractions of Mg and Fe end-members in olivine, X_{Fe}^{M1}, X_{Fe}^{M2} are the atomic fraction of Fe in the two different orthopyroxene sites (M1 and M2), and $a_{Fe_3O_4}^{sp}$ is the activity of Fe_3O_4 in spinel. The results yield upper limits for values of fO_2 as charge-balanced normalization yields the maximum value of $Fe^{3+}/\Sigma Fe$ for spinel composition as described in the previous section (see the ANALYTICAL PROCEDURE section above). Estimated values of fO_2 are given in Table 9.

Table 9. Oxygen fugacity estimates

Sample	$\Delta\log(fO_2)^{FMQ}$
NRTP4	-2.18
DS0260	-3.19
DS0286	-1.98
NUM9a	-1.76

8. FLUID EQUILIBRIA IN THE C-O-H SYSTEM

A number of researchers have used fluid equilibria to constrain activities of six different fluid species- H_2O, CO_2, CH_4, H_2, CO, and O_2 – in the graphite/diamond bearing C-O-H system (French, 1966; Ohmoto and Kerrick, 1977; Lamb and Valley, 1984, 1985). These six fluid species are related by four different reactions:

$$C + O_2 = CO_2 \quad (5)$$

$$C + \frac{1}{2}O_2 = CO \quad (6)$$

$$H_2 + \frac{1}{2}O_2 = H_2O \quad (7)$$

$$CH_4 + 2O_2 = CO_2 + 2H_2O \quad (8)$$

Simultaneous solution of these four equilibria can yield the activities of these six fluid species in a graphite or diamond bearing rock by assuming that free fluid is present such that:

$$P_{lith} = P_{fluid} = P_{H_2O} + P_{CO_2} + P_{CH_4} + P_{CO} + P_{H_2} + P_{O_2} \quad (9)$$

where P_{lith} equals to the lithostatic pressure.

In this study, the free energy minimization approach described by Zhang and Duan (2009) was used to constrain the activities of seven fluid species, which includes above-mentioned six fluid species as well as C_2H_6. Additional species of C_2H_6 adds to the number of equilibria to be considered including the above-mentioned four different equilibria as well as the following:

$$2C + 3H_2 = C_2H_6 \quad (10)$$

This approach also relies on the same assumption of $P_{lith} = P_{fluid}$ as previous methods, but in this case, the partial pressure of C_2H_6 would contribute to the total fluid pressure, such that:

$$P_{lith} = P_{fluid} = P_{H_2O} + P_{CO_2} + P_{CH_4} + P_{CO} + P_{H_2} + P_{O_2} + P_{C_2H_6} \quad (11)$$

As a comparison, we also used the computer program CalCOH (Lamb, 1987) described by Lamb and Valley (1984, 1985) to estimate the activities of the six fluid species listed in equation (9).

Calculation of fluid speciation has typically been performed in carbon (i.e. graphite or diamond) bearing system such that aC is unity. However, as first demonstrated by Lamb and Valley (1984), these calculations can be performed for systems that do not contain graphite or diamond, and in this case the result provides limits on the activities of various fluid species. For example, calculations which assume that aC = 1 maximizes the activities of carbon-bearing species, such as CO_2, CH_4, and CO, while simultaneously minimizing the activities of the non-carbon-bearing species, such as H_2O (Lamb and Valley, 1984, 1985). This result is illustrated by Figure 18 which shows the activities of four fluid species are plotted as a function of $\Delta\log(fO_2)^{FMQ}$ at aC = 1 and aC = 0.01 (Activities of CO and C_2H_6 are omitted from this figure for clarity as these are never greater than 0.001 over the range of fO_2 values shown in this figure). Regardless of the values of aC, the relative positions of three major species, CH_4, H_2O, and CO_2, are similar. CO_2 dominates under relatively oxidizing condition and CH_4 becomes predominant under reducing conditions with H_2O dominant under intermediate range of fO_2. Reducing the value of carbon activity (e.g., to aC = 0.01) expands the

range of fO_2 over which the non carbon bearing species H_2O is the dominant fluid species at the expense of carbon bearing species, such as CO_2 and CH_4 (Fig. 18). The extended range of H_2O predominance is accompanied with higher estimate of aH_2O at a given value of $\Delta\log(fO_2)^{FMQ}$ (Fig. 18). This is consistent with the previous results that show using aC = 1 for C-O-H equilibria calculation provides the minimum possible amount of H_2O in the C-O-H system at any given value of fO_2 (Lamb and Valley, 1984, 1985).

a)

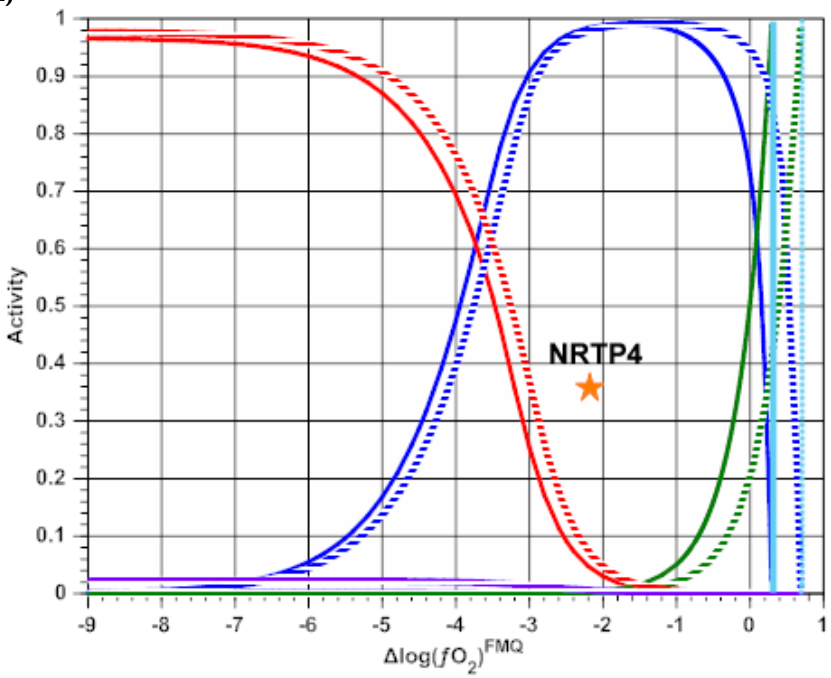

Figure 18. Activities of four different fluid species in C-O-H system at aC = 1 (a) and aC = 0.01 (b) at a pressure of 24kbar and temperature of 720˚C. Solid lines and dotted lines indicate the results of calculations based on C-O-H equilibria using the approach of Zhang and Duan (2009) and Lamb and Valley (1985) respectively. The estimate of aH_2O obtained from pargasite dehydration equilibrium is plotted together at $\Delta\log(fO_2)^{FMQ}$ of the sample (NRTP4) determined from Wood's oxybarometer. The difference in estimates of aH_2O between pargasite dehydration equilibrium and C-O-H equilibria becomes greater at aC = 0.01. The vertical lines in each diagram are located at $\Delta\log(fO_2)^{FMQ}$ beyond which aC becomes less than a given value of 1 and 0.01 respectively.

b)

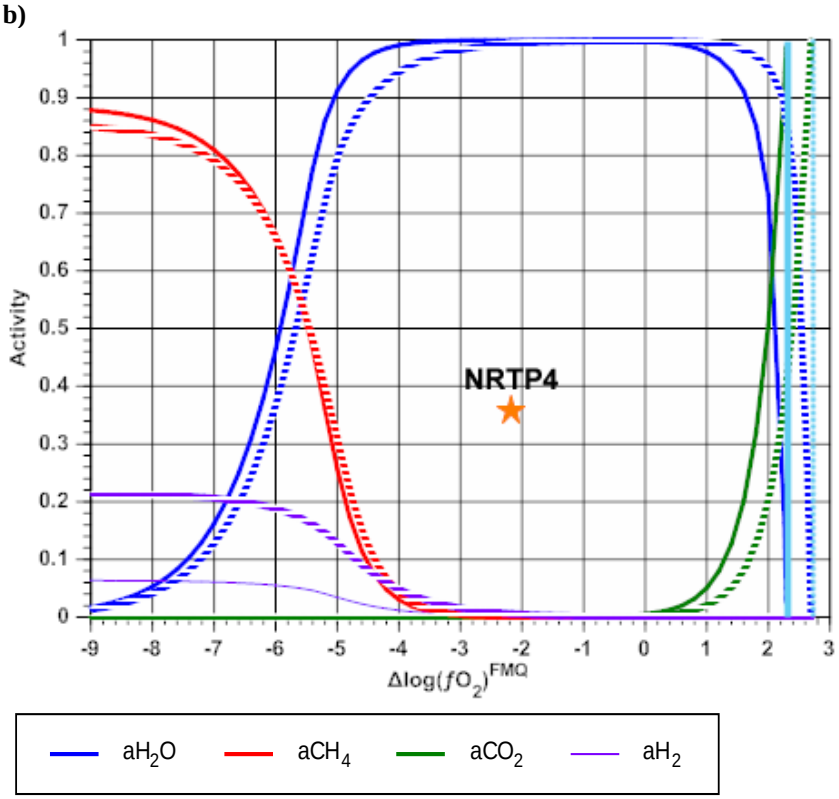

Figure 18 Continued.

Results of minimum estimates of aH_2O obtained from these two different approaches (i.e., Zhang and Duan, 2009 and Lamb and Valley, 1984, 1985) were compared with estimates of aH_2O derived from pargasite dehydration equilibrium in Table 10. This comparison shows that minimum estimates of aH_2O determined from C-O-H calculations are significantly higher than those from pargasite dehydration equlibrium. The inconsistency between values of aH_2O as determined from two different methods, C-O-H equilibria and amphibole equilibria, is illustrated by plotting the value of aH_2O estimated from amphibole equilibria at defined $\Delta\log(fO_2)^{FMQ}$ on the diagram that results from the C-O-H calculations (Fig. 18).

Table 10. H_2O activities estimated from amphibole dehydration equilibrium and two different C-O-H calculations with aC = 1

Sample	aH_2O (Dehydration)	aH_2O (Zhang & Duan, 2009)	aH_2O (Lamb & Valley, 1985)
NRTP4	0.36	0.96	0.95
DS0260	0.26	0.88	0.90
DS0286	0.23	0.95	0.90
NUM9a	0.12	0.99	0.95

Since changing the value of aC cannot resolve the inconsistency between values of aH_2O, it follows that the assumption of a lithostatically pressured C-O-H fluid phase must be inappropriate (Lamb and Valley, 1984, 1985). There are two possible ways to resolve this situation: (1) If $P_{fluid} = P_{lith}$, the fluid must contain a significant amount of non C-O-H components (e.g., H_2S or N_2), or (2) $P_{fluid} < P_{lith}$. In the second case, C-O-H equilibria calculations can satisfy all mathematical constraints and yield aH_2O as low as those obtained from pargasite dehydration equilibrium. The value of pressure required to yield such low aH_2O for each sample is less than 1kbar, which is significantly lower than P_{lith}. However, it has been argued that P_{fluid} must be equivalent to P_{lith} in high grade, ductile rocks (Walther and Orville, 1982; Walther and Wood, 1984; Wood and Walther, 1986). If that is the case, then the situation in which $P_{fluid} < P_{lith}$ may indicate that a free fluid is not present (fluid absence) at the time of mineral equilibration (Lamb and Valley, 1984, 1985). In the absence of evidence for significant non C-O-H fluid components, inconsistent estimates of aH_2O likely indicate fluid-absent condition during mineral equilibration at the estimated values of P and T.

9. CONCLUSION

Amphiboles in the samples of this study grew relatively late, as compared to other matrix minerals, during the exhumation stages of the Western Gneiss Region of Norway. The formation of these amphiboles suggests that H_2O was available during the uplift stages to support the growth of the hydrous phase of amphibole. However, our estimation of aH_2O based on pargasite dehydration equilibrium yield values that are significantly less than 1. If small amounts of H_2O were added to these rocks, amphibole formation could consume this H_2O and be stabilized at low values of aH_2O. This mechanism is consistent with the vapor-absent condition suggested by the calculations in the C-O-H system ($P_{fluid} < P_{lith}$). If the infiltrating fluid contained fluid species other than H_2O then the consumption of H_2O to produce amphibole could make the fluid enriched in other fluid species. In this case, the fluid must have contained a significant amount of non-C-O-H components (e.g., H_2S and N_2), as the possibility of a fluid dominated by CO_2 or CH_4 is ruled out by the C-O-H calculations at fO_2 that were defined for our samples (Fig. 18; Table 10).

It is possible that this infiltration of H_2O occurred prior to the formation of amphibole perhaps at P-T conditions outside of the stability field of amphibole. In this case, H_2O may have been stored in co-existing NAMs instead of amphibole. Given that the solubility of H within NAMs significantly decreases with decreasing pressure (Kohlstedt et al., 1996; Mosenfelder et al., 2006), if H is present within NAMs at high pressures then depressurization that accompanied exhumation will yield increased values

of aH_2O. This combination of lower pressures and increased values of aH_2O might have stabilized amphibole. Therefore, it is possible that all the H required for amphibole growth was provided by co-existing NAMs, a process that should reduce the H-content of NAMs. If this were the case, the growth of amphibole may effectively dehydrate co-existing NAMs. In this scenario, the growth of amphibole could enhance the strength of rocks by removing H from NAMs as long as the NAMs were volumetrically dominant such that they continued to control the rheology of the rock.

REFERENCES

Asimow, P.D. and Ghiorso, M.S., 1998, Algorithmic modifications extending MELTS to calculate subsolidus phase relations, American Mineralogist, 83(9-10), p. 1127-1132.

Bai, Q. and Kohlstedt, D.L., 1992, Substantial hydrogen solubility in olivine and implications for water storage in the mantle, Nature, 357(6380), p. 672-674.

Bai, Q. and Kohlstedt, D.L., 1993, Effects of chemical environment on the solubility and incorporation mechanism for hydrogen in olivine, Physics and Chemistry of Minerals, 19(7), p. 460-471.

Bell, D.R., Rossman, G.R., Maldener, J., Endisch, D., and Rauch, F., 2003, Hydroxide in olivine: a quantitative determination of the absolute amount and calibration of the IR spectrum, Journal of Geophysical Research: Solid Earth, 108(B2), p. ECV 8-1-8-9.

Brey, G.P. and Köhler, T., 1990, Geothermobarometry in four-phase lherzolites II. New thermobarometers, and practical assessment of existing thermobarometers, Journal of Petrology, 31(6), p. 1353-1378.

Brueckner, H.K., Carswell, D.A., and Griffin, W.L., 2002, Paleozoic diamonds within a Precambrian peridotite lens in UHP gneisses of the Norwegian Caledonides, Earth and Planetary Science Letters, 203(3-4), p. 805-816.

Canil, D. and O'Neill, H.S.C., 1996, Distribution of ferric iron in some upper-mantle assemblages, Journal of Petrology, 37(3), p. 609-635.

Carswell, D.A., 1986, The metamorphic evolution of Mg-Cr type Norwegian garnet peridotites, Lithos, 19(3-4), p. 279-297.

Carswell, D.A. and Van Roermund, H.L.M., 2005, On multi-phase mineral inclusions associated with microdiamond formation in mantle-derived peridotite lens at Bardane on Fjørtoft, west Norway, European Journal of Mineralogy, 17(1), p. 31-42.

Cuthbert, S.J., Carswell, D.A., Krogh-Ravna, E.J., and Wain, A., 2000, Eclogites and eclogites in the Western Gneiss Region, Norwegian Caledonides, Lithos, 52(1-4), p. 165-195.

Dale, J., Powell, R., White, R.W., Elmer, F.L., and Holland, T.J.B., 2005, A thermodynamic model for Ca-Na clinoamphiboles in Na_2O-CaO-FeO-MgO-Al_2O_3-SiO_2-H_2O-O for petrological calculations, Journal of Metamorphic Geology, 23(8), p. 771-791.

Demouchy, S. and Mackwell, S., 2006, Mechanisms of hydrogen incorporation and diffusion in iron-bearing olivine, Physics and Chemistry of Minerals, 33(5), p. 347-355.

Duan, Z., Møller, N., and Weare, J.H., 1992, Molecular dynamics simulation of PVT properties of geological fluids and a general equation of state of nonpolar and weakly polar gases up to 2000K and 20000 bar, Geochimica et Cosmochimica Acta, 56(10), p. 3839-3845.

Duan, Z., Møller, N., and Weare, J.H., 1996, A general equation of state for supercritical fluid mixtures and molecular dynamics simulation of mixture PVTX properties, Geochimica et Cosmochimica Acta, 60(7), p. 1209-1216.

French, B.M., 1966, Some geological implications of equilibrium between graphite and a C-H-O gas phase at high temperatures and pressures, Reviews of Geophysics, 4(2), p. 223-253.

Ghiorso, M.S. and Evans, B.W., 2002, Thermodynamics of the amphiboles: Ca-Mg-Fe^{2+} quadrilateral, American Mineralogist, 87(1), p. 79-98.

Ghiorso, M.S. and Sack, R.O., 1995, Chemical mass transfer in magmatic processes IV. A revised and internally consistent thermodynamic model for the interpolation and extrapolation of liquid-solid equilibria in magmatic systems at elevated-temperatures and pressures, Contributions to Mineralogy and Petrology, 119(2-3), p. 197-212.

Green, D.H. and Ringwood, A.E., 1970, Mineralogy of peridotitic compositions under upper mantle conditions, Physics of the Earth and Planetary Interiors, 3(0), p. 359-371.

Grütter, H.S., 2009, Pyroxene xenocryst geotherms: techniques and application, Lithos, 112(0), p. 1167-1178.

Grütter, H., Latti, D., and Menzies, A., 2006, Cr-saturation arrays in concentrate garnet compositions from kimberlite and their use in mantle barometry, Journal of Petrology, 47(4), p. 801-820.

Hirth, G. and Kohlstedt, D.L., 1996, Water in the oceanic upper mantle: implications for rheology, melt extraction and the evolution of the lithosphere, Earth and Planetary Science Letters, 144(1-2), p. 93-108.

Ingrin, J. and Skogby, H., 2000, Hydrogen in nominally anhydrous upper-mantle minerals concentration levels and implications, European Journal of Mineralogy, 12(3), p. 543-570.

Karato, S. and Jung, H., 2003, Effects of pressure on high-temperature dislocation creep in olivine polycrystals, Philosophical Magazine A, 83(3), p. 401-414.

Klemme, S., 2004, The influence of Cr on the garnet-spinel transition in the Earth's mantle: experiments in the system MgO-Cr_2O_3-SiO_2 and thermodynamic modeling, Lithos, 77(1-4), p. 639-646.

Kohlstedt, D.L. and Mackwell, S.J., 1998, Diffusion of hydrogen and intrinsic point defects in olivine, Zeitschrift für Physikalische Chemie, 207(1-2), p. 147-162.

Koyama, T., Shimizu, H., Utada, H., Ichiki, M., Ohtani, E., and Hae, R., 2006, Water contents in the mantle transition zone beneath the North Pacific derived from the electrical conductivity anomaly, in Earth's Deep Water Cycle (eds Jacobsen, S.D. and Van Der Lee, S.F.M.), American Geophysical Union, Washington, D. C., p. 171-179.

Kress, V.C., Ghiorso, M.S., and Lastuka, C., 2004, Microsoft EXCEL spreadsheet-based program for calculating equilibrium gas speciation in the C-O-H-S-Cl-F system, Computers & Geosciences, 30(3), p. 211-214.

Lamb, W. and Popp, R., 2009, Amphibole equilibria in mantle rocks: determining values of mantle aH_2O contents, American Mineralogist, 94(1), p. 41-52.

Lamb, W. and Valley, J.W., 1984, Metamorphism of reduced granulites in low-CO_2 vapour-free environment, Nature, 312(5989), p. 56-58.

Lamb, W. and Valley, J.W., 1985, C-O-H fluid calculations and granulite genesis, in The Deep Proterozoic Crust in the North Atlantic Provinces (eds Tobi, A.C. and Touret, J.L.R.), D. Reidel Publishing Company, Dordrecht, p. 119-131.

Lamb, W. and Valley, J.W., 1987, Post-metamorphic CO_2 rich inclusion in granulites, Contributions to Mineralogy and Petrology, 96(4), p. 485-495.

Maldener, J., Hösch, A., Langer, K., and Rauch, F., 2003, Hydrogen in some natural garnets studied by nuclear reaction analysis and vibrational spectroscopy, Physics and Chemistry of Minerals, 30(6), p. 337-344.

Medaris Jr, L.G., 1984, A geothermobarometric investigation of garnet peridotites in the Western Gneiss Region of Norway, Contributions to Mineralogy and Petrology, 87(1), p. 72-86.

Mei, S. and Kohlstedt, D.L., 2000a, Influence of water on plastic deformation of olivine aggregates: 1. Diffusion creep regime, Journal of Geophysical Research: Solid Earth, 105(B9), p. 21457-21469.

Mei, S. and Kohlstedt, D.L., 2000b, Influence of water on plastic deformation of olivine aggregates: 2. Dislocation creep regime, Journal of Geophysical Research: Solid Earth, 105(B9), p. 21471-21481.

Moresi, L. and Solomatov, V., 1998, Mantle convection with a brittle lithosphere: thoughts on the global tectonic styles of the Earth and Venus, Geophysical Journal International, 133(3), p. 669-682.

Mosenfelder, J.L., Deligne, N.I., Asimow, P.D., and Rossman, G.R., 2006, Hydrogen incorporation in olivine from 2-12 GPa, American Mineralogist, 91(2-3), p. 285-294.

Nickel, K.G. and Green, D.H., 1985, Empirical geothermobarometry for garnet peridotites and implications for the nature of the lithosphere, kimberlites and diamonds, Earth and Planetary Science Letters, 73(1), p. 158-170.

Nimis, P. and Grütter, H., 2010, Internally consistent geothermometers for garnet peridotites and pyroxenites, Contributions to Mineralogy and Petrology, 159(3), p. 411-427.

Nimis, P. and Taylor, W.R., 2000, Single clinopyroxene thermobarometry for garnet peridotities. Part I. Calibration and testing of a Cr-in-Cpx barometer and an enstatite-in-Cpx thermometer, Contributions to Mineralogy and Petrology, 139(5), p. 541-554.

Obata, M. and Ozawa, K., 2011, Topotaxic relationships between spinel and pyroxene in kelyphite after garnet in mantle-derived peridotites and their implications to reaction mechanism and kinetics, Mineralogy and Petrology, 101(3-4), p. 217-224.

Ohmoto, H. and Kerrick, D.M., 1977, Devolatilization equilibria in graphitic systems, American Journal of Science, 277(8), p. 1013-1044.

O'Neill, H.S.C., 1980, An experimental study of Fe-Mg-partitioning between garnet and olivine and its calibration as a geothermometer: corrections, Contributions to Mineralogy and Petrology, 72(3), p. 337.

O'Neill, H.S.C. and Wood, B.J., 1979, An experimental study of Fe-Mg partitioning between garnet and olivine and its calibration as a geothermometer, Contributions to Mineralogy and Petrology, 70(1), p. 59-70.

Peslier, A.H., Luhr, J.F., and Post, J., 2002, Low water contents in pyroxenes from spinel-peridotites of the oxidized, sub-arc mantle wedge, Earth and Planetary Science Letters, 201(1), p. 69-86.

Popp, R.K., Hibbert, H.A., and Lamb, W.M., 2006a, Erratum: oxy-amphibole equilibria in Ti-bearing calcic amphiboles: experimental investigation and petrologic implications for mantle-derived amphiboles by R.K. Popp, H.A. Hibbert, and W.M. Lamb (vol. 91, no. 1, p. 54-66, DOI: 10.2138/am.2006.1838), American Mineralogist, 91(4), p. 716.

Popp, R.K., Hibbert, H.A., and Lamb, W.M., 2006b, Oxy-amphibole equilibria in Ti-bearing calcic amphiboles: experimental investigation and petrologic implications for mantle-derived amphiboles, American Mineralogist, 91(1), p. 54-66.

Roberts, D. and Gee, D.G., 1985, An introduction to the structure of the Scandinavian Caledonides, in The Caledonide Orogen-Scandinavia and related areas (eds Gee, D.G. and Sturt, B.A.), John Wiley & Sons, Chichester, p. 55-68.

Skogby, H., Bell, D.R., and Rossman, G.R., 1990, Hydroxide in pyroxene: variations in the natural environment, American Mineralogist, 75(7-8), p. 764-774.

Smith, D.C., 1984, Coesite in clinopyroxene in the Caledonides and its implications for geodynamics, Nature, 310(5979), p. 641–644.

Solomatov, V.S., 1995, Scaling of temperature- and stress-dependent viscosity convection, Physics of Fluids, 7(2), p. 266-274.

Spengler, D., Brueckner, H.K., Van Roermund, H.L.M., Drury, M.R., and Mason, P.R.D., 2009, Long-lived, cold burial of Baltica to 200 km depth, Earth and Planetary Science Letters, 281(1-2), p. 27-35.

Spengler, D., Van Roermund, H.L.M., Drury, M.R., Ottolini, L., Mason, P.R.D., and Davies, G.R., 2006, Deep origin and hot melting of an Archaean orogenic peridotite massif in Norway, Nature, 440(7086), p. 913-917.

Tackley, P.J., 1998, Self-consistent generation of tectonic plates in three-dimensional mantle convection, Earth and Planetary Science Letters, 157(1-2), p. 9-22.

Tarits, P., Hautot, S., and Perrier, F., 2004, Water in the mantle: results from electrical conductivity beneath the French Alps, Geophysical Research Letters, 31(6), p. L06612 1-5.

Taylor, W.R., 1998, An experimental test of some geothermometer and geobarometer formulations for upper mantle peridotites with application to the thermobarometry of fertile lherzolite and garnet websterite, Neues Jahrbuch für Mineralogie-Abhandlungen, 172(2-3), p. 381-408.

Van Roermund, H., 2009, Mantle-wedge garnet peridotites from the northernmost ultra-high pressure domain of the Western Gneiss Region, SW Norway, European Journal of Mineralogy, 21(6), p. 1085-1096.

Van Roermund, H.L.M., Carswell, D.A., Drury, M.R., and Heijboer, T.C., 2002, Microdiamonds in a megacrystic garnet websterite pod from Bardane on the island of

Fjørtoft, western Norway: evidence for diamond formation in mantle rocks during deep continental subduction, Geology, 30(11), p. 959-962.

Vrijmoed, J.C., Van Roermund, H.L.M., and Davies, G.R., 2006, Evidence for diamond-grade ultra-high pressure metamorphism and fluid interaction in the Svartberget Fe-Ti garnet peridotite-websterite body, Western Gneiss Region, Norway, Mineralogy and Petrology, 88(1-2), p. 381-405.

Walther, J.V. and Orville, P.M., 1982, Volatile production and transport in regional metamorphism, Contributions to Mineralogy and Petrology, 79(3), p. 252-257.

Walther, J.V. and Wood, B.J., 1984, Rate and mechanism in prograde metamorphism, Contributions to Mineralogy and Petrology, 88(3), p. 246-259.

Warren, J.M. and Hauri, E.H., 2014, Pyroxenes as tracers of mantle water variations, Journal of Geophysical Research: Solid Earth, 119(3), p. 1851-1881.

Wood, B.J., 1990, An experimental test of the spinel peridotite oxygen barometer, Journal of Geophysical Research, 95(B10), p. 15845-15851.

Wood, B.J., 1995, The effect of H_2O on the 410-kilometer seismic discontinuity, Science, 268(5207), p. 74-76.

Wood, B.J. and Walther, J.V., 1986, Fluid flow during metamorphism and its implications for fluid-rock ratios, in Fluid-Rock Interactions During Metamorphism, (eds Walther, J.V. and Wood, B.J.), Springer-Verlag, New York, p. 89-108.

Wood, B.J. and Virgo, D., 1989, Upper mantle oxidation state: Ferric iron contents of lherzolite spinels by ^{57}Fe Mössbauer spectroscopy and resultant oxygen fugacities, Geochimica et Cosmochimica Acta, 53(6), p. 1277-1291.

Woodland, A.B., Kornprobst, J., and Wood, B.J., 1992, Oxygen thermobarometry of orogenic lherzolite massifs, Journal of Petrology, 33(1), p. 203-230.

Wu, C.M. and Zhao, G.C., 2007, A recalibration of the garnet-olivine geothermometer and a new geobarometer for garnet peridotites and garnet-olivine-plagioclase-bearing granulites, Journal of Metamorphic Geology, 25(5), p. 497-505.

Zhang, C. and Duan, Z., 2009, A model for C-O-H fluid in the Earth's mantle, Geochimica et Cosmochimica Acta, 73(7), p. 2089-2102.

Zhang, C. and Duan, Z., 2010, GFluid: an Excel spreadsheet for investigating C-O-H fluid composition under high temperatures and pressures, Computers & Geosciences, 36(4), p. 569-572.

APPENDIX A

The procedure used to normalize amphibole formulae is described in Lamb and Popp (2009). The value of $Fe^{3+}/\Sigma Fe$, where $\Sigma Fe = Fe^{3+} + Fe^{2+}$, required to apply this procedure, was not determined independently for the samples in this study. We chose to assume the minimum ratio of $Fe^{3+}/\Sigma Fe$ that produced a charge-balanced formula. This assumption should yield an amphibole formula with the maximum possible OH-content as the OH content of the amphibole will increase with decreasing values of $Fe^{3+}/\Sigma Fe$ as shown by

$$Ca_2Fe_5^{2+}Si_8O_{22}(OH)_2 = Ca_2Fe_3^{2+}Fe_2^{3+}Si_8O_{22}(O^{2-})_2 + H_2 \quad (A.1)$$

Given a (minimum) value of $Fe^{3+}/\Sigma Fe$, amphibole was initially normalized to a total number of O atoms (Lamb and Popp, 2009). The resulting cation contents were then used with one of the two empirical relations (Popp et al., 1995a; King et al. 1999) that quantify the correlation between oxy/hydroxy components on the Z-site and cation contents on other crystallographic sites in order to define the amount of oxy component. One of the relations indicates that the amount of substitution of O^{2-} for OH^-, Cl^-, and F^- on the Z-site (oxy component) can be quantified by the sum of Fe^{3+} and Ti^{4+} (Popp et al., 1995a). This relation, which can be written as $O^{2-} = Fe^{3+} + Ti^{4+}$, when combined with the equation describing the Z-site occupancy, i.e., $2.0 = \square + OH^- + Cl^- + F^-$ (where $\square$ indicates the oxy component), can be written as (Popp et al., 1995a):

$$2.0 = (Fe^{3+} + Ti^{4+}) + OH^- + Cl^- + F^{-2} \quad (A.2)$$

The other relation is similar but considers Al^{VI} as well as Ti and Fe^{3+}, in the correlation between the O^{2-} content on the Z-site with cation contents on other crystallographic sites, and is given by (King et al., 1999):

$$Fe^{3+} = 2.47 - 0.93(OH) - \left(Ti + Al^{VI}\right) \quad (A.3)$$

This relation, when combined with the equation for the Z-site occupancy ($2.0 = \square + OH^- + Cl^- + F^-$), can also be used to define the amount of oxy component.

To determine a charge balanced formula, the total number of cations determined by the oxygen-based normalization was decreased in small increments until the total positive charge became equal to the total negative charge. During this iterative process, relative proportions of cations were kept constant while satisfying their site-occupancy constraints, as described by Lamb and Popp (2009). In each iteration, any readjustment in the amount of Fe^{3+}, Ti^{4+}, and Al^{VI} caused by reducing the total number of cations would change the amount of oxy component and therefore the total negative charge. Therefore, as the total number of cations was continuously reduced, the total negative charge was simultaneously adjusted. This iterative normalization procedure consequently yielded the total number of cations in the amphibole formula, which was in turn used to define the vacancies on the A-site.

APPENDIX B

Table B 1. Microprobe analyses of representative garnets in the samples of this study indicated via oxide wt% and normalized cations per formula unit

Garnet											
	NUM9a			DS0286		DS0260			NRTP4		
	Core	Cr-dip	Rim	Core	Rim(Cr-dip)	Core	Cr-increase	Right Rim (Cr-dip)	Core	Cr-dip	Rim
SiO_2	41.87	41.92	41.82	41.33	41.43	41.16	41.02	40.80	42.31	42.26	42.10
Al_2O_3	21.64	23.41	23.00	22.14	22.05	19.72	19.33	19.64	21.87	22.42	22.08
TiO_2	0.01	0.02	0.02	0.00	0.00	0.00	0.03	0.00	0.20	0.12	0.04
Cr_2O_3	3.91	1.50	1.93	2.81	3.10	5.82	6.41	6.08	3.43	2.78	3.07
FeO	7.47	8.55	9.73	9.26	9.13	8.09	7.95	9.42	8.74	10.14	10.63
MnO	0.41	0.57	0.77	0.48	0.55	0.53	0.48	0.69	0.43	0.55	0.70
MgO	19.59	19.24	18.83	19.08	19.39	17.12	16.76	16.06	19.42	18.87	18.40
CaO	5.41	4.87	4.46	4.98	4.60	8.15	8.58	8.01	5.87	5.44	5.43
Sum	100.31	100.08	100.55	100.07	100.25	100.57	100.54	100.70	102.27	102.58	102.44
$Si^{(IV)}$	2.99	2.99	2.98	2.96	2.96	2.98	2.98	2.98	2.97	2.97	2.97
$Al^{(IV)}$	0.01	0.01	0.02	0.04	0.04	0.02	0.02	0.03	0.03	0.03	0.03
$Al^{(VI)}$	1.81	1.96	1.92	1.83	1.82	1.66	1.64	1.66	1.78	1.83	1.81
Ti	0.00	0.00	0.00	0.00	0.00	0.00	0.00	0.00	0.01	0.01	0.00
Cr	0.22	0.09	0.11	0.16	0.18	0.33	0.37	0.35	0.19	0.16	0.17
Fe^{3+}	0.00	0.00	0.00	0.04	0.04	0.02	0.02	0.01	0.03	0.04	0.04
Fe^{2+}	0.45	0.51	0.58	0.51	0.51	0.47	0.47	0.56	0.48	0.56	0.59
Mn	0.03	0.03	0.05	0.03	0.03	0.03	0.03	0.04	0.03	0.03	0.04
Mg	2.08	2.04	2.00	2.04	2.07	1.85	1.82	1.75	2.03	1.98	1.94
Ca	0.41	0.37	0.34	0.38	0.35	0.63	0.67	0.63	0.44	0.41	0.41
Sum	8.00	8.00	8.00	8.00	8.00	8.00	8.00	8.00	8.00	8.00	8.00

Table B 2. Microprobe analyses of representative spinels in the samples of this study indicated via oxide wt% and normalized cations per formula unit

	Spinel							
	NUM9a		DS0286		DS0260		NRTP4	
	Core	Rim	Core	Rim	Core	Rim	Core	Rim
SiO_2	0.00	0.02	0.00	0.00	0.00	0.00	0.01	0.02
Al_2O_3	16.66	28.03	25.07	26.66	22.35	25.00	19.07	25.87
TiO_2	0.00	0.00	0.00	0.00	0.08	0.00	0.07	0.06
Cr_2O_3	52.69	41.19	43.57	41.48	47.80	44.94	49.68	42.54
V_2O_3	0.13	0.17	0.19	0.18	0.16	0.19	0.17	0.19
FeO	19.21	16.60	18.27	17.70	18.41	18.29	20.03	18.39
MnO	0.50	0.38	0.42	0.44	0.32	0.35	0.41	0.31
MgO	10.03	13.18	11.38	11.86	11.35	11.82	10.01	11.90
CaO	0.01	0.01	0.00	0.00	0.00	0.00	0.00	0.00
NiO	0.01	0.04	0.00	0.00	0.02	0.00	0.00	0.00
ZnO	0.26	0.26	0.00	0.00	0.12	0.00	0.00	0.10
Sum	99.50	99.89	98.89	98.32	100.61	100.58	99.45	99.38
Si	0.00	0.00	0.00	0.00	0.00	0.00	0.00	0.00
Al	0.63	0.98	0.92	0.97	0.82	0.90	0.72	0.93
Ti	0.00	0.00	0.00	0.00	0.00	0.00	0.00	0.00
Cr	1.34	0.98	1.07	1.01	1.17	1.08	1.25	1.03
V	0.00	0.00	0.01	0.00	0.00	0.01	0.00	0.01
Fe^{3+}	0.03	0.03	0.01	0.01	0.01	0.01	0.02	0.01
Fe^{2+}	0.49	0.39	0.46	0.44	0.47	0.45	0.52	0.46
Mn	0.01	0.01	0.01	0.01	0.01	0.01	0.01	0.01
Mg	0.48	0.59	0.53	0.55	0.52	0.54	0.48	0.54
Ca	0.00	0.00	0.00	0.00	0.00	0.00	0.00	0.00
Ni	0.00	0.00	0.00	0.00	0.00	0.00	0.00	0.00
Zn	0.02	0.02	0.00	0.00	0.00	0.00	0.00	0.00
Sum	3.00	3.00	3.00	3.00	3.00	3.00	3.00	3.00

Table B 3. Microprobe analyses of representative orthopyroxenes in the samples of this study indicated via oxide wt% and normalized cations per formula unit

Orthopyroxene												
	NUM9a		DS0286		DS0260		NRTP4		COR		Kelyphite	
	Core	Rim	Core	Rim	Core	Rim	Core	Rim	Adjacent to kelyphite	Adjacent to the matrix	Adjacent to garnet	Adjacent to the matrix
SiO_2	58.64	58.36	57.40	56.35	57.45	57.18	58.53	57.80	56.32	57.36	50.04	56.04
Al_2O_3	0.32	0.82	0.56	1.70	0.96	1.12	0.64	1.00	2.51	1.10	10.58	2.69
TiO_2	0.01	0.00	0.00	0.00	0.01	0.02	0.01	0.00	0.00	0.00	0.00	0.00
Cr_2O_3	0.09	0.17	0.15	0.22	0.18	0.14	0.13	0.17	0.13	0.00	1.11	0.23
FeO	4.61	4.78	5.37	5.79	6.19	6.29	5.41	6.03	6.22	5.89	6.58	6.28
MnO	0.10	0.12	0.09	0.24	0.17	0.20	0.10	0.19	0.00	0.26	0.21	0.27
MgO	36.29	35.74	34.88	33.66	34.62	34.45	36.15	35.47	33.61	33.99	32.08	33.64
CaO	0.10	0.16	0.12	0.22	0.17	0.19	0.15	0.18	0.22	0.19	0.15	0.21
NiO	0.09	0.04	0.00	0.00	0.07	0.05	0.00	0.00	0.00	0.11	0.00	0.00
Na_2O	0.01	0.02	0.01	0.00	0.01	0.01	0.00	0.00	0.00	0.00	0.00	0.00
K_2O	0.01	0.01	0.00	0.00	0.00	0.00	0.00	0.00	0.00	0.00	0.00	0.00
Sum	100.27	100.22	98.58	99.25	99.81	99.66	101.11	100.83	99.01	98.90	100.74	99.35
$Si^{(IV)}$	2.00	1.99	2.00	1.98	1.98	1.98	1.98	1.97	1.96	2.00	1.71	1.95
$Al^{(IV)}$	0.00	0.01	0.00	0.02	0.02	0.02	0.02	0.03	0.04	0.00	0.29	0.06
$Al^{(VI)}$	0.01	0.03	0.02	0.05	0.02	0.02	0.01	0.01	0.06	0.05	0.14	0.06
Ti	0.00	0.00	0.00	0.00	0.00	0.00	0.00	0.00	0.00	0.00	0.00	0.00
Cr	0.00	0.01	0.00	0.01	0.01	0.00	0.00	0.00	0.00	0.00	0.03	0.01
Fe^{3+}	0.00	0.00	0.00	0.00	0.00	0.00	0.01	0.02	0.00	0.00	0.12	0.00
Fe^{2+}	0.13	0.14	0.16	0.17	0.18	0.18	0.15	0.16	0.18	0.17	0.06	0.18
Mn	0.00	0.00	0.00	0.01	0.01	0.01	0.00	0.01	0.00	0.01	0.01	0.01
Mg	1.84	1.82	1.81	1.76	1.78	1.78	1.83	1.80	1.74	1.77	1.63	1.74
Ca	0.00	0.01	0.01	0.01	0.01	0.01	0.01	0.01	0.01	0.01	0.01	0.01
Ni	0.00	0.00	0.00	0.00	0.00	0.00	0.00	0.00	0.00	0.00	0.00	0.00
Na	0.00	0.00	0.00	0.00	0.00	0.00	0.00	0.00	0.00	0.00	0.00	0.00
Sum	4.00	4.00	4.00	4.00	4.00	4.00	4.00	4.00	4.00	4.00	4.00	4.00

Table B 4. Microprobe analyses of representative clinopyroxenes in the samples of this study indicated via oxide wt% and normalized cations per formula unit

Clinopyroxene											
	NUM9a		DS0286		DS0260		NRTP4		Cpx replaced by Amp	Kelyphite	
	Core	Rim	Core	Rim	Core	Rim	Core	Rim	Average	Adjacent to garnet	Adjacent to the matrix
SiO_2	55.37	55.14	53.57	54.03	55.40	55.50	54.86	54.84	54.53	49.82	53.44
Al_2O_3	0.00	0.03	1.59	1.35	1.51	1.36	1.73	0.96	1.30	5.66	2.24
TiO_2	2.76	1.81	0.00	0.00	0.00	0.00	0.00	0.00	0.06	0.24	0.14
Cr_2O_3	2.42	0.96	1.24	0.55	0.93	0.66	1.52	0.34	0.78	0.66	0.43
FeO	0.99	1.28	1.33	1.49	1.34	1.42	1.37	1.58	1.40	1.94	1.56
MnO	0.07	0.05	0.02	0.12	0.00	0.00	0.00	0.00	0.00	0.00	0.00
MgO	0.06	0.04	17.30	17.86	17.43	17.85	17.01	18.09	17.70	17.69	17.31
CaO	15.36	17.03	24.37	24.61	23.46	23.79	22.85	24.51	24.02	23.25	24.79
NiO	20.84	22.95	0.00	0.00	0.00	0.00	0.00	0.00	0.00	0.00	0.00
Na_2O	2.34	1.07	0.38	0.17	0.91	0.64	1.10	0.30	0.54	0.10	0.12
K_2O	0.02	0.01	0.00	0.00	0.00	0.00	0.00	0.00	0.00	0.00	0.00
Sum	100.20	100.36	99.82	100.18	100.96	101.21	100.43	100.61	100.34	99.35	100.03
$Si^{(IV)}$	1.99	1.98	1.94	1.95	1.98	1.98	1.97	1.97	1.96	1.81	1.94
$Al^{(IV)}$	0.01	0.02	0.06	0.05	0.02	0.02	0.03	0.03	0.04	0.19	0.06
$Al^{(VI)}$	0.11	0.06	0.01	0.01	0.04	0.04	0.05	0.01	0.02	0.05	0.03
Ti	0.00	0.00	0.00	0.00	0.00	0.00	0.00	0.00	0.00	0.01	0.00
Cr	0.07	0.03	0.04	0.02	0.03	0.02	0.04	0.01	0.02	0.02	0.01
Fe^{3+}	0.00	0.01	0.03	0.04	0.01	0.01	0.01	0.03	0.03	0.06	0.02
Fe^{2+}	0.03	0.03	0.01	0.01	0.03	0.03	0.03	0.02	0.02	0.00	0.03
Mn	0.00	0.00	0.00	0.00	0.00	0.00	0.00	0.00	0.00	0.00	0.00
Mg	0.82	0.91	0.94	0.96	0.93	0.95	0.91	0.97	0.95	0.96	0.94
Ca	0.80	0.88	0.95	0.95	0.90	0.91	0.88	0.94	0.93	0.90	0.96
Ni	0.00	0.00	0.00	0.00	0.00	0.00	0.00	0.00	0.00	0.00	0.00
Na	0.16	0.07	0.03	0.01	0.06	0.04	0.08	0.02	0.04	0.01	0.01
K	0.00	0.00	0.00	0.00	0.00	0.00	0.00	0.00	0.00	0.00	0.00
Sum	4.00	4.00	4.00	4.00	4.00	4.00	4.00	4.00	4.00	4.00	4.00

Table B 5. Microprobe analyses of representative matrix amphiboles in the samples of this study indicated via oxide wt%

Amphibole								
	NUM9a		DS0286		DS0260		NRTP4	
	Core	Rim (Adjacent to kelyphite)	Core	Rim (Adjacent to kelyphite)	Core	Rim (Adjacent to kelyphite)	Core	Rim (Adjacent to kelyphite)
SiO_2	46.64	43.79	45.99	45.59	45.06	45.27	45.35	45.17
Al_2O_3	12.78	15.62	13.32	13.67	13.57	13.57	13.15	14.79
TiO_2	0.06	0.03	0.00	0.00	0.13	0.13	0.39	0.14
Cr_2O_3	1.83	2.93	2.05	1.77	1.99	2.03	2.18	1.47
FeO	2.19	2.50	2.31	2.60	2.92	2.71	2.31	2.73
MnO	0.09	0.13	0.00	0.00	0.06	0.05	0.00	0.00
MgO	20.02	18.70	19.26	19.03	19.06	19.03	18.89	17.51
CaO	11.35	11.14	12.69	12.48	12.06	12.23	12.52	12.31
NiO	0.06	0.08	0.09	0.00	0.12	0.13	0.00	0.00
Na_2O	3.21	3.68	2.16	2.21	2.78	2.78	2.29	2.23
K_2O	0.11	0.03	0.00	0.00	0.10	0.08	0.29	0.00
Sum	98.33	98.62	97.88	97.35	97.84	98.01	97.35	96.35

Table B 6. Results of normalization for matrix amphiboles using the empirical relations of Ox = Ti+Fe and Ox = (Fe^{3+}/0.93)-0.65591-(F#+Cl#)+((Ti+AlM_{123})/0.93), which are indicated as 1 and 2 respectively

Amphibole																
	NUM9a				DS0286				DS0260				NRTP4			
	Core		Rim (Adjacent to kelyphite)		Core		Rim (Adjacent to kelyphite)		Core		Rim (Adjacent to kelyphite)		Core		Rim (Adjacent to kelyphite)	
	1	2	1	2	1	2	1	2	1	2	1	2	1	2	1	2
$Si^{(IV)}$	6.49	6.49	6.13	6.15	6.43	6.44	6.41	6.43	6.35	6.35	6.36	6.36	6.41	6.41	6.41	6.46
$Al^{(IV)}$	1.51	1.51	1.87	1.86	1.57	1.56	1.59	1.57	1.65	1.65	1.64	1.64	1.59	1.59	1.59	1.54
$Ti^{(M123)}$	0.01	0.01	0.00	0.00	0.00	0.00	0.00	0.00	0.01	0.01	0.01	0.01	0.04	0.04	0.02	0.02
$Al^{(M123)}$	0.59	0.59	0.70	0.73	0.63	0.64	0.68	0.70	0.61	0.61	0.61	0.61	0.60	0.60	0.88	0.95
$Cr^{(M123)}$	0.20	0.20	0.32	0.33	0.23	0.23	0.20	0.20	0.22	0.22	0.23	0.23	0.25	0.25	0.17	0.17
$Fe^{3+(M123)}$	0.00	0.00	0.00	0.00	0.00	0.00	0.00	0.00	0.00	0.00	0.00	0.00	0.00	0.00	0.00	0.00
$Fe^{2+(M123)}$	0.04	0.05	0.06	0.02	0.11	0.11	0.13	0.11	0.15	0.15	0.15	0.16	0.14	0.15	0.24	0.13
$Mg^{(M123)}$	4.15	4.15	3.90	3.91	4.02	4.02	3.99	4.00	4.01	4.01	3.99	3.99	3.97	3.97	3.70	3.73
$Mn^{(M123)}$	0.00	0.00	0.00	0.00	0.00	0.00	0.00	0.00	0.00	0.00	0.00	0.00	0.00	0.00	0.00	0.00
$Ni^{(M123)}$	0.01	0.01	0.01	0.01	0.01	0.01	0.00	0.00	0.00	0.00	0.01	0.01	0.00	0.00	0.00	0.00
$Mg^{(M4)}$	0.00	0.00	0.00	0.00	0.00	0.00	0.00	0.00	0.00	0.00	0.00	0.00	0.00	0.00	0.00	0.00
$Fe^{2+(M4)}$	0.21	0.21	0.23	0.27	0.16	0.17	0.17	0.20	0.19	0.19	0.17	0.16	0.13	0.13	0.09	0.19
$Mn^{(M4)}$	0.01	0.01	0.02	0.02	0.00	0.00	0.00	0.00	0.00	0.00	0.01	0.01	0.00	0.00	0.00	0.00
$Ca^{(M4)}$	1.69	1.69	1.67	1.68	1.84	1.84	1.83	1.80	1.81	1.81	1.83	1.83	1.87	1.87	1.87	1.81
$Na^{(M4)}$	0.09	0.09	0.08	0.04	0.00	0.00	0.00	0.00	0.00	0.00	0.00	0.00	0.00	0.00	0.04	0.00
$Ca^{(A)}$	0.00	0.00	0.00	0.00	0.06	0.07	0.05	0.09	0.01	0.01	0.01	0.01	0.01	0.01	0.00	0.08
$Na^{(A)}$	0.78	0.78	0.92	0.96	0.59	0.59	0.60	0.60	0.76	0.76	0.76	0.76	0.63	0.63	0.57	0.62
$K^{(A)}$	0.02	0.02	0.01	0.01	0.00	0.00	0.00	0.00	0.02	0.02	0.01	0.01	0.06	0.06	0.00	0.00
Vac	0.20	0.20	0.08	0.04	0.35	0.34	0.34	0.31	0.21	0.21	0.22	0.22	0.31	0.31	0.43	0.30
F	0.00	0.00	0.00	0.00	0.00	0.00	0.00	0.00	0.00	0.00	0.00	0.00	0.00	0.00	0.00	0.00
Cl	0.00	0.00	0.00	0.00	0.00	0.00	0.00	0.00	0.00	0.00	0.00	0.00	0.00	0.00	0.00	0.00
O	0.01	0.00	0.00	0.13	0.00	0.03	0.00	0.09	0.01	0.01	0.01	0.01	0.04	0.03	0.02	0.38
OH	1.99	2.00	2.00	1.87	2.00	1.97	2.00	1.91	1.99	1.99	1.99	1.99	1.96	1.97	1.99	1.62

Table B 7. Microprobe analyses of fine-grained amphiboles within the kelyphite as well as matrix amphibole in NRTP4, indicated via oxide wt%. Matrix amphibole texturally replaces matrix clinopyroxene

Amphibole			
	Amp replacing Cpx	**Kelyphite**	
	Average	**Adjacent to garnet**	**Adjacent to the matrix**
SiO_2	45.82	44.61	44.54
Al_2O_3	12.74	14.64	14.71
TiO_2	0.34	0.28	0.28
Cr_2O_3	2.02	1.89	2.09
FeO	2.56	2.92	2.83
MnO	0.00	0.07	0.06
MgO	19.63	18.34	18.18
CaO	12.28	12.50	12.43
NiO	0.00	0.05	0.09
Na_2O	2.57	2.24	2.37
K_2O	0.10	0.05	0.03
Sum	98.05	97.57	97.61

Table B 8. Results of normalization for matrix amphiboles which replaces matrix clinopyroxenes and fine-grained amphiboles within the kelyphite in NRTP4 using two empirical relations of Ox = Ti+Fe and Ox = $(Fe^{3+}/0.93)$-0.65591-(F#+Cl#)+$((Ti+AlM_{123})/0.93)$ which are indicated as 1 and 2 respectively

Amphibole						
	Amp replacing Cpx		**Kelyphite**			
	Average		**Adjacent to garnet**		**Adjacent to the matrix**	
	1	2	1	2	1	2
$Si^{(IV)}$	6.42	6.42	6.29	6.31	6.28	6.30
$Al^{(IV)}$	1.58	1.58	1.71	1.69	1.72	1.70
$Ti^{(M123)}$	0.04	0.04	0.03	0.03	0.03	0.03
$Al^{(M123)}$	0.53	0.52	0.72	0.75	0.73	0.76
$Cr^{(M123)}$	0.22	0.22	0.21	0.21	0.23	0.23
$Fe^{3+(M123)}$	0.00	0.00	0.00	0.00	0.00	0.00
$Fe^{2+(M123)}$	0.11	0.12	0.18	0.13	0.18	0.14
$Mg^{(M123)}$	4.10	4.10	3.85	3.87	3.82	3.84
$Mn^{(M123)}$	0.00	0.00	0.00	0.00	0.00	0.00
$Ni^{(M123)}$	0.00	0.00	0.01	0.01	0.01	0.01
$Mg^{(M4)}$	0.00	0.00	0.00	0.00	0.00	0.00
$Fe^{2+(M4)}$	0.19	0.18	0.17	0.21	0.15	0.20
$Mn^{(M4)}$	0.00	0.00	0.01	0.01	0.01	0.01
$Ca^{(M4)}$	1.81	1.82	1.83	1.78	1.84	1.79
$Na^{(M4)}$	0.00	0.00	0.00	0.00	0.00	0.00
$Ca^{(A)}$	0.04	0.02	0.06	0.12	0.04	0.09
$Na^{(A)}$	0.70	0.70	0.61	0.61	0.65	0.65
$K^{(A)}$	0.02	0.02	0.01	0.01	0.01	0.01
Vac	0.25	0.26	0.32	0.26	0.31	0.25
F	0.00	0.00	0.00	0.00	0.00	0.00
Cl	0.00	0.00	0.00	0.00	0.00	0.00
O	0.04	0.00	0.03	0.19	0.03	0.19
OH	1.96	2.00	1.97	1.82	1.97	1.81

Table B 9. Microprobe analyses of representative olivines in the samples of this study indicated via oxide wt% and normalized cations per formula unit

Olivine				
	NUM9a (Average)	**DS0286 (Average)**	**DS0260 (Average)**	**NRTP4 (Average)**
SiO_2	40.86	40.97	41.15	41.14
Al_2O_3	0.00	0.00	0.13	0.00
FeO	7.26	7.67	9.30	8.34
MnO	0.08	0.12	0.18	0.11
MgO	51.13	50.39	49.09	50.68
CaO	0.01	0.01	0.01	0.00
NiO	0.41	0.42	0.42	0.41
Na_2O	0.01	0.00	0.01	0.01
Sum	99.75	99.58	100.29	100.68
Si	0.99	1.00	1.01	1.00
Al	0.00	0.00	0.00	0.00
Fe^{2+}	0.15	0.16	0.19	0.17
Mn	0.00	0.00	0.00	0.00
Mg	1.85	1.83	1.79	1.83
Ca	0.00	0.00	0.00	0.00
Ni	0.01	0.01	0.01	0.01
Na	0.00	0.00	0.00	0.00
Sum	3.00	3.00	3.00	3.00